

Feasibility and Accuracy of Thermophysical Estimation of Asteroid 162173 Ryugu (1999 JU3) from the Hayabusa2 Thermal Infrared Imager

Jun Takita^{1,2} · Hiroki Senshu³ · Satoshi Tanaka²

Received: 22 August 2015 / Accepted: 25 January 2017 / Published online: 27 February 2017
© Springer Science+Business Media Dordrecht 2017

Abstract We present the results of a numerical study to prepare for the remote sensing of asteroid 162173 Ryugu (1999 JU3) using the Hayabusa2 thermal infrared imager (TIR). We simulated the thermal characteristics of the asteroid with a thermophysical model (TPM) using an ideal body with a smooth and spherical surface, and investigated its feasibility to determine the thermophysical properties of the asteroid under two possible spin vectors; $(\lambda_{\text{ec1}}, \beta_{\text{ec1}}) = (73^\circ, -62^\circ)$ and $(331^\circ, 20^\circ)$. Each of the simulated snapshots taken at various local times during the 1.5-year proximity phase was analyzed to estimate uncertainties of the diurnal thermal phase delay to infer the thermal inertia of Ryugu. The temperature in a pixel was simulated based on the specification of the imager and the observing geometry. Moreover, we carried out a regression analysis to estimate albedo and thermal emissivity from the time variation of surface temperature. We also investigated the feasibility of determining thermal phase delay in a first attempt using realistic rough surfaces. We found that precise determination of the thermal phase delay would be difficult in the $(331^\circ, 20^\circ)$ spin type unless the surface was nearly smooth. In contrast, the thermal phase delay is likely to be observable even if the surface topography is moderately rough in the other spin type. From the smooth-surface model, we obtained a less than 20% error of thermal inertia on observation opportunities under the likely range of thermal inertia $\leq 1000 \text{ J m}^{-2} \text{ s}^{-1/2} \text{ K}^{-1}$. The error of thermal inertia exceeded 50% under a realistic surface with roughness.

Keywords Near earth asteroid · Thermo-physical properties · TIR · Hayabusa2

✉ J. Takita
takita@planeta.sci.isas.jaxa.jp

¹ University of Tokyo, Bunkyo-ku, Tokyo, Japan

² Institute of Space and Astronautical Science, Japan Aerospace Exploration Agency, Sagami-hara, Kanagawa, Japan

³ Chiba Institute of Technology, Narashino, Chiba, Japan

1 Introduction

The thermophysical properties of near-earth asteroids (NEAs) have gained much attention since the discovery that thermal inertia can provide insight into the physical state of planetary surfaces. Thermal inertia, $\Gamma = \sqrt{\rho ck}$ (where ρ is density, c is specific heat, and k is thermal conductivity), controls the temperature distribution over a surface to provide volumetric information within the scale length of heat diffusion. Therefore, the thermal inertia can be a sensitive indicator for the nature of the regolith on the surface of asteroids, in particular of the grain size. The latter can be affected by the global size and the age of a body: e.g. Delbó et al. (2007) and Gundlach and Blum (2013) show how thermal inertia depends on the asteroid size. Big bodies, with their stronger gravitational potential, can keep more easily than small asteroids the ejecta of impacts that, falling back on the body, form the regolith (Horz and Cintala 1997). However, bigger asteroids have longer gravitational collisional lifetime than smaller ones, and thus have more time to develop a finer regolith via both impact (Horz and Cintala 1997) and thermal cracking (Delbó et al. 2014) processes. In this respect, thermal inertia might be used as a measure of the age of an asteroid.

Moreover, thermal inertia affects the strength of the Yarkovsky effect, which induces orbital change (Vokrouhlický et al. 2000; Chesley et al. 2003; Delbó et al. 2007). Thermal inertia can be used to infer the strength of Yarkovsky and YORP-induced thermal torque, which in turn is useful for investigating the interior structure of an asteroid (Lowry et al. 2014).

Knowledge of an asteroid's thermal inertia has been acquired using disk-integrated measurements. The thermal inertia of more than 50 asteroids is known at present (see e.g. Delbó et al. 2015, and the references therein). These values provide spatially averaged results. Extensive ground-based observations cover the thermal inertia of the trans-Neptunian objects, the Centaurus and Kuiper belt objects, from Herschel and Spitzer observations (average $2.5 \text{ J m}^{-2} \text{ s}^{-1/2} \text{ K}^{-1}$) (Lellouch et al. 2013). For more distant objects, the thermal inertia of the Pluto system was observed by the Spitzer observatory; thermal inertia was determined to be 20 to $30 \text{ J m}^{-2} \text{ s}^{-1/2} \text{ K}^{-1}$ for Pluto and 10 to $150 \text{ J m}^{-2} \text{ s}^{-1/2} \text{ K}^{-1}$ for Charon (Lellouch et al. 2011). The New Horizons spacecraft flew by the multiple system in July 2015 (Stern et al. 2015). Pluto's surface displays diversity in geological features and evidence is found for a water-ice crust (Stern et al. 2015).

Interplanetary missions can provide disk-resolved images of the targets to derive the thermal inertia of the planetary surface where ground-based observations have difficulty obtaining spatial resolutions. For example, regional maps of thermal inertia on Mars have been presented, and the thermophysical structures of the Martian surface have been derived based on remote-sensing results (Mellon et al. 2000; Putzig et al. 2005; Ferguson et al. 2006; Audouard et al. 2014). Thermal inertia has been used to discriminate exposed bedrocks on Mars from regolith since Γ is known to be higher for dense material such as bedrock. Similarly, rock abundance on the lunar surface was estimated using thermal properties attributable to surface heterogeneities based on observations using the Diviner Radiometer data from the Lunar Reconnaissance Orbiter (e.g., Bandfield et al. 2011; Paige et al. 2010).

The thermal inertia of Phobos and Deimos, the Martian moons, were measured in the Mariner 9 mission using the infrared radiometer, which showed extremely low conductive layer of dust covered the surface of Phobos (Gatley et al. 1974). The subsequent Viking orbiter (Lunine et al. 1982) and the Phobos-2 spacecraft measured the thermophysical properties of the satellites (Ksanfomality et al. 1989, 1991; Kührt et al. 1992), suggesting a lunar-like regolith texture.

Thermophysical observation of the solid planets in the outer solar system includes performance on Jovian and Saturnian satellites. The thermal inertias of four Galilean satellites, which were observed by the Voyager and the Galileo spacecraft, were estimated to be 50 to $70 \text{ J m}^{-2} \text{ s}^{-1/2} \text{ K}^{-1}$ (Spencer 1987; Spencer et al. 1999; Rathbun et al. 2004). The thermal inertia of the Saturnian moons (Mimas, Enceladus, Tethys, Dione, Rhea, and Iapetus) was derived from the data of the Cassini spacecraft. The thermal inertias of these satellites were 2 to 6 times lower than those of the Galilean satellites, which implied a less consolidated and more porous surface (Howett et al. 2010). Moreover, from the mid-infrared spectra of Phoebe, the mean thermal inertia was determined to be $20 \text{ J m}^{-2} \text{ s}^{-1/2} \text{ K}^{-1}$. The low thermal inertia for solid water ice was assumed to imply a highly fragmented regolith (Flasar et al. 2005).

As for small bodies, the thermal inertia of Comet 9P/Tempel 1 was estimated to be less than $200 \text{ J m}^{-2} \text{ s}^{-1/2} \text{ K}^{-1}$ during the flyby of the Deep Impact mission and the subsequent EPOXI mission, which also observed the Comet 103P/Hartley2 ($< 250 \text{ J m}^{-2} \text{ s}^{-1/2} \text{ K}^{-1}$) (Groussin et al. 2007, 2013). The disentanglement of thermal inertia and surface roughness is discussed in the works of Davidsson et al. (2009, 2013).

The Rosetta spacecraft observed the thermal inertia of the Comet 67P/Churyumov-Gerasimenko (10 to $50 \text{ J m}^{-2} \text{ s}^{-1/2} \text{ K}^{-1}$) (Gulkis et al. 2015). Moreover, the Rosetta lander Philae measured the thermal inertia of the landing site using an infrared radiometer at 50 to $120 \text{ J m}^{-2} \text{ s}^{-1/2} \text{ K}^{-1}$ (Spohn et al. 2015), which was higher than the representative value of the overall surface.

Asteroid 21 Lutetia and 2867 Steins were observed in the flyby of the Rosetta spacecraft before arrival at the comet. Very low thermal inertia was required to explain the observations of Lutetia: less than 20 to $40 \text{ J m}^{-2} \text{ s}^{-1/2} \text{ K}^{-1}$, which is comparable to that of a lunar-like powdery regolith (Gulkis et al. 2012; Coradini et al. 2011). The low thermal inertia of the asteroid Lutetia is also supported by the work through the Herschel Space Observatory (O'Rourke et al. 2012). In the analysis of the thermal inertia of Steins, surface roughness was studied using thermal modeling. The results confirm that surface roughness affects the derivation of thermal inertia: $110 \text{ J m}^{-2} \text{ s}^{-1/2} \text{ K}^{-1}$ for a smooth surface and $210 \text{ J m}^{-2} \text{ s}^{-1/2} \text{ K}^{-1}$ for a rough surface (Leyrat et al. 2011).

The Dawn spacecraft measured thermal infrared emission from asteroid 4 Vesta. Thermal inertia of $30 \text{ J m}^{-2} \text{ s}^{-1/2} \text{ K}^{-1}$ was derived from the retrieved temperature (Capria et al. 2014). Extremely low thermal inertia ($< 5 \text{ J m}^{-2} \text{ s}^{-1/2} \text{ K}^{-1}$) and high surface roughness were also indicated in a crater region (Keihm et al. 2015). These values are consistent with the typical thermal inertias for large main-belt asteroids (1 Ceres, 2 Pallas, 4 Vesta and 532 Herculina): 5 to $25 \text{ J m}^{-2} \text{ s}^{-1/2} \text{ K}^{-1}$, which are derived from Infrared Space Observatory (Müller and Lagerros 1998; Müller et al. 1999), and are smaller than the lunar value: $50 \text{ J m}^{-2} \text{ s}^{-1/2} \text{ K}^{-1}$ (Spencer et al. 1989).

The previous Hayabusa mission indicated that asteroid 25143 Itokawa had a boulder-rich surface. Although no directional thermal measurement was performed in remote sensing to derive thermal inertia, this finding was consistent with the high thermal inertia of Itokawa ($750 \text{ J m}^{-2} \text{ s}^{-1/2} \text{ K}^{-1}$) (Müller et al. 2005), which was derived from ground-based observation.

Plans for the Hayabusa2 mission include monitoring the surface of the near earth asteroid 162173 Ryugu within several tens of meters resolution. The spacecraft will reach the asteroid in mid-2018 and perform operations for 1.5 years (Tsuda et al. 2013). Asteroid Ryugu is classified as C-type in the taxonomy (Vilas 2008), and the surface of Ryugu can be considered homogeneous in ground-based estimation from the time series of visible spectra (Moskovitz et al. 2013). Some fundamental properties of the asteroid were estimated using ground observations in the works of Hasegawa et al. (2008), Abe et al. (2008),

Campins et al. (2009), and Müller et al. (2011). While estimations of optical properties (e.g., albedo, H-G parameter, rotational period, and radius) were determined precisely, the value of thermal inertia and the solution of the spin vector remain unclear. The observed value of I of Ryugu ranges from 150 to 900 $\text{J m}^{-2} \text{s}^{-1/2} \text{K}^{-1}$, based on the works of Hasegawa et al. (2008), Campins et al. (2009), and Müller et al. (2011). While the spin vector solution $\lambda_{\text{ecl}} = 331^\circ$, $\beta_{\text{ecl}} = 20^\circ$ in a study by Abe et al. (2008), Müller et al. (2011) analyze both spin axis solutions and strongly prefer a retrograde sense of rotation with a spin-axis orientation of $\lambda_{\text{ecl}} = 73^\circ$, $\beta_{\text{ecl}} = -62^\circ$, and $P_{\text{sid}} = 7.63 \pm 0.01$ hr. The retrograde rotation is also consistent with an origin of Ryugu from ν 6 secular resonance, as pointed out by Campins et al. (2013).

As for upcoming spacecraft missions, the OSIRIS-REx will return samples from the near earth asteroid, 101955 Benu (Lauretta 2012). Benu is classified as B-type in the taxonomy which includes 2 Pallas, the second largest main-belt asteroid. The mission will carry OSIRIS-REx Thermal Emission Spectrometer (OTES) which provides mineral and thermal emission spectral maps in 4–50 μm . The data can be used to derive temperature maps of the asteroid surface, from which maps of thermal inertia and surface roughness can be deduced. The disk-averaged thermal inertia of Benu is 240 to 380 $\text{J m}^{-2} \text{s}^{-1/2} \text{K}^{-1}$ (Emery et al. 2014).

2 Operation of Hayabusa2 TIR and Its Strategy

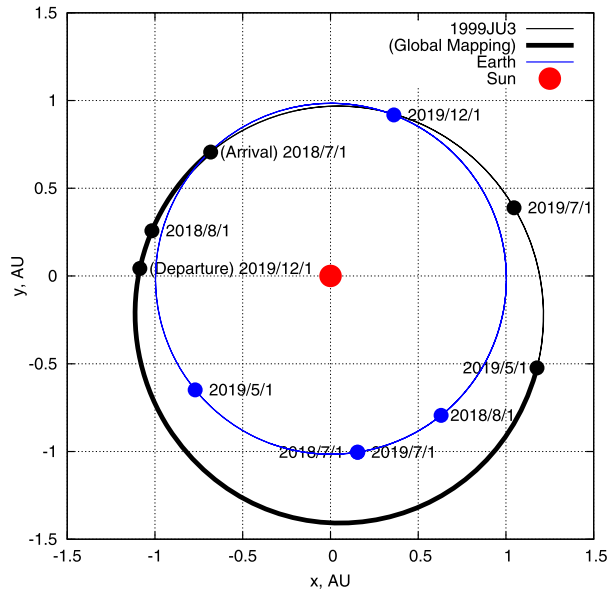
2.1 Outline of the TIR Imager Operations

The main objective of Hayabusa2 is to obtain samples from the asteroid surface as well as to perform scientific observations using remote-sensing devices. To observe the thermal inertia of the target asteroid, the spacecraft deploys a thermal infrared imager (TIR), which provides information of candidate sample sites and can support safe operation for the sample return by monitoring the in-situ surface temperature of the target asteroid. Thermal inertia is needed to predict surface temperature in the future, and is estimated from TIR observation. The Hayabusa2 TIR inherited the longwave infrared camera onboard the Venus orbiter Akatsuki (Fukuhara et al. 2012). As an image sensor, the TIR has a micro-bolometer that covers 8 to 12 μm . The basic specifications of Hayabusa2 TIR are listed in Table 1 (see Okada et al. 2015 for more detail). The detectable range of the temperature of the TIR is 150 to 460 K. The TIR was calibrated in a thermally controlled environment using a black-body plate whose temperature and infrared emissivity were known. When the temperature of monitored objects is 233 to 423 K, the absolute temperature accuracy of the TIR is less than 3 K and

Table 1 Brief description of the Hayabusa2 TIR imager

Item	Specifications
Wave length	8–12 μm
Field of view	16 \times 12 deg
Pixel number	328 \times 248
Spatial resolution	0.05 deg/pix (0.9 mrad/pix)
Temperature range	233–423 K (150–460 K, detectable)
Temperature resolution	< 3 K (absolute) < 0.3 K (relative)

Fig. 1 Orbit diagram during the operational term of the Hayabusa2 mission in the heliocentric ecliptic plane. The spacecraft is planned to reach the target asteroid in July 2018 (Tsuda et al. 2013). The global mapping is an in-situ observation phase to determine not only the global shape of the asteroid, the rotational period, and the orientation of the spin axis, but also the global temperature and the composition of surface materials. The term after May 2019 is a backup margin of the global mapping phase to cover extra observations. The spacecraft will leave the asteroid in December 2019 to return to the Earth



the relative accuracy is less than 0.3 K, based on the noise equivalent temperature difference (Okada et al. 2015).

Thermophysical studies of the target asteroid will begin from a distance of 2000 km with a space where the TIR will detect disk-integrated thermal emissions from the asteroid and measure its thermal infrared lightcurve. After arrival, Hayabusa2 will stay at a nominal position (target distance 20 to 40 km), positioning a satellite antenna in the sub-earth direction to communicate with the Earth. The spacecraft will stay at this position and will not orbit the asteroid. The observation will continue for 1.5 years, and the TIR will map the global surface temperature of the target asteroid (Fig. 1). During this mapping phase, the solar array panel will be oriented toward the sun. Thus, the dayside surface of the asteroid will be monitored mainly by onboard instruments, which are attached to the main body of the spacecraft in the opposite direction of the solar panel. While S/N of the TIR is worse in low temperature target < 233 K, this will not cause a significant error in the dayside observation from the TIR.

The target distance of the spacecraft is 20 km with a space in the global mapping phase. The spatial resolution of the target asteroid from the TIR will be 20 m/pixel at this altitude. The TIR plans to observe the asteroid once a week in nominal operation after arrival at the asteroid, and target images will be taken every 512 sec in a single performance of the TIR. We will obtain 50 images of the asteroid in a single rotation of 7.63 hr. Therefore, each of the surface elements (area within the field of view (FOV) of the TIR) will be seen every 7 degrees for the rotational angle. This phase also includes low-altitude observation and touchdown observation, and the surface temperature of the local areas during these operations will be observed using the TIR (Okada et al. 2015).

2.2 Strategy for Estimating Thermal Inertia Under Restricted Operation

Thermal inertia measures the tendency of an object to resist change in surface temperature. The surface temperature of material with high thermal inertia does not change as fast as

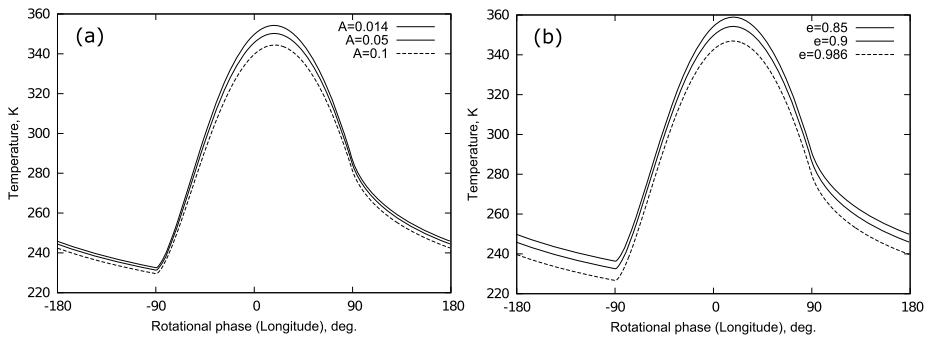


Fig. 2 Examples to illustrate that albedo and emissivity do not affect the amount of thermal phase delay in diurnal motion. **(a)** Thermal emissivity is 0.9. **(b)** Bond albedo is 0.014. The thermal inertia of the curves is $400 \text{ J m}^{-2} \text{ s}^{-1/2} \text{ K}^{-1}$. These properties of thermal profiles are valid for different thermal inertia

that of material with low thermal inertia, which easily responds to transient changes of the external thermal state. Finite thermal inertia requires corresponding time delay to change the surface temperature. Hence, thermal inertia can be estimated in terms of the degree of time delay.

For planetary surfaces, thermal inertia can be inferred from nighttime temperature profiles (e.g., Linsky 1966; Keihm and Langseth 1973; Bandfield et al. 2011; Vasavada et al. 2012). The diurnal profile of the surface temperature of a planet and its amplitude of temperature change between night and day can also be utilized to infer thermal inertia, whose methods were used in estimating the thermal inertia of Jovian and Saturnian satellites (Spencer et al. 1999; Rathbun et al. 2004; Flasar et al. 2005; Howett et al. 2010). For the Hayabusa2 mission, the spacecraft is not an orbiter, and the remote-sensing instruments onboard will face mainly on the day side during proximity operation, except for optional operation such as high phase angle observation (Okada et al. 2015). Thus, a whole temperature curve in a rotation of the asteroid will not always be retrieved during the observation.

The degree of maximum surface temperature can provide firsthand information related to the thermal inertia of a planetary surface, although the maximum temperature could be affected by other thermophysical properties (e.g., bond albedo, thermal emissivity, and surface roughness). In contrast, thermal phase delay of a diurnal temperature profile is not strongly affected by these values (Fig. 2). This approach requires only dayside temperatures. Considering these restrictions in the observation, we selected this approach to deduce thermal inertia.

In this study, we investigated the feasibility and accuracy using an ideal body whose surface is smooth and spherical to prepare for mission operations on thermophysical estimation. We used numerical methods to evaluate the observations of Ryugu from realistically simulated images of the asteroid seen from the spacecraft, in an effort to find a period of opportunity to observe thermal inertia during the 1.5-year operational term. Included is a description of the derivation of albedo and emissivity using surface temperature data. Moreover, we discuss the feasibility of thermophysical estimation using some realistic rough surfaces, as a preliminary study for more advanced studies in our future work.

3 Method

3.1 Thermal Modeling of Asteroid

The thermal models of asteroids have different implementations of thermal behavior. The thermophysical model (TPM) treats finite thermal inertia explicitly to solve the heat conduction problem under the boundary conditions on a planetary surface (Spencer et al. 1989; Lagerros 1996, 1997, 1998). Our thermal model is categorized as this type. We calculate time evolutions of surface temperature in our numerical model. Asteroid Ryugu is presently estimated to be spherical (Müller et al. 2011) rather than a shape that strongly requires multipolygonal configuration, like asteroid Itokawa. We adopted spherical geometry to construct our thermal model.

We calculated the position of asteroid Ryugu in the heliocentric ecliptic coordinate system (J2000EC) with the orbital elements. The heliocentric distance changes from 0.964 to 1.416 AU in the orbit. The spin vector of Ryugu has not been clearly constrained from ground-based observations, due to its rounded shape. We adopted two types of spin vector solution in our thermal models: $(\lambda_{\text{ecl}}, \beta_{\text{ecl}}) = (73^\circ, -62^\circ)$ and $(331^\circ, 20^\circ)$ where λ_{ecl} and β_{ecl} are the components of the spin vector in the ecliptic coordinates. These values are based on results observed by Müller et al. (2011) and Abe et al. (2008). The spin pole plays an important role in the TPM (Hanusš et al. 2015).

We adopted bond albedo $A = 0.014$ from the ground-based observations of Ishiguro et al. (2014). We assumed emissivity $\epsilon = 0.9$, which is commonly used in Hasegawa et al. (2008), Campins et al. (2009), and Müller et al. (2011). While mid-infrared emissivity (8–12 μm) is generally greater than 0.9 (near 1.0) based on measurement of the reflectance of Carbonaceous meteorites (e.g., ASTER Spectral Library (Baldrige et al. 2009)), we assumed that the effect of emissivity on thermophysical estimation is negligible for the shift of thermal curves (e.g., Fig. 2). Besides, significant emission features are not seen in the wavelength range of the TIR from the Spitzer spectrum of Ryugu (Campins et al. 2009).

The thermophysical properties such as specific heat and thermal conductivity are generally functions of temperature. Density is a function of depth. These functions of lunar soil were studied using lunar samples (see e.g., Appendix of Keihm 1984). Indeed, temperature dependence plays an important role in explaining the behavior of the nighttime temperature of lunar regolith (Vasavada et al. 2012). However, for dayside observation of Hayabusa2, the temperature near the sub-solar region does not change over several tens of Kelvin (e.g., 20 K in the profiles of $\Gamma = 400 \text{ J m}^{-2} \text{ s}^{-1/2} \text{ K}^{-1}$), which might not cause a significant error for thermophysical estimation from the phase shift. We assumed materials were uniformly distributed in the medium and their thermal properties were constant against temperature variation.

3.2 Thermal Equation and Boundary Conditions

The thermal state of an asteroid surface in the TPM is usually implemented using the unsteady 1D heat conduction equation under the boundary conditions of solar irradiance and thermal emission from the surface. This is based on the assumption that the thermal diffusion scale is small enough to neglect lateral heat conduction. The heat conduction equation in the absence of internal heat sources is

$$\frac{\partial T}{\partial t} = \frac{k}{\rho c} \frac{\partial^2 T}{\partial z^2}, \quad (1)$$

Table 2 Model parameters of the standard case in numerical calculations

Fixed parameters	Value	Source
Radius of asteroid	450 m	Typical value of †
Rotational period	7.36 hr	Hasegawa et al. (2008)
Bond albedo	0.014	Ishiguro et al. (2014)
Emissivity	0.9	Common value of †
Density	1662 kg m ⁻³	Opeil et al. (2010)
Specific heat	700 J kg ⁻¹ K ⁻¹	Yomogida and Matsui (1983)
(Orbital elements)		JPL Small Body Database Browser
Semi-major axis	1.19 AU	
Eccentricity	0.19	
Inclination of revolution orbit	5.9°	
Longitude of ascending node	251.6°	
Argument of perihelion	211.4°	
Time of perihelion passage	2456376.1351 JED	
Free parameters	Symbol	Model values
Thermal inertia	Γ	0, 200, 400, 600, 1000 J m ⁻² s ^{-1/2} K ⁻¹
Spin vector	($\lambda_{\text{ecl}}, \beta_{\text{ecl}}$)	(73°, -62°), (331°, 20°)

† (Hasegawa et al. 2008; Abe et al. 2008; Campins et al. 2009; Müller et al. 2011)

Table 3 Symbols and definitions

S_0	Solar constant	W m ⁻²	1370
σ	Stephan-Boltzmann constant	W m ⁻² K ⁻⁴	5.67 × 10 ⁻⁸
c_0	Speed of light	m s ⁻¹	3.00 × 10 ⁸
h	Planck constant	J s	6.63 × 10 ⁻³⁴
k_B	Boltzmann constant	J K ⁻¹	1.38 × 10 ⁻²³

where ρ is density, c is specific heat, and k is thermal conductivity. Tables 2 and 3 list the constants used in this study.

The surface boundary conditions are given by

$$(1 - A)F_S(t) = -k \frac{\partial T}{\partial z} \Big|_{z=0} + \varepsilon \sigma T_{z=0}^4, \tag{2}$$

where A is bond albedo, $F_S(t)$ is the time-dependent flux of incident sunlight, ε is emissivity, and σ is the Stefan-Boltzmann constant. The boundary condition at the bottom is given by

$$\frac{\partial T}{\partial z} \Big|_{z=z_0} = 0, \tag{3}$$

where z_0 is the bottom depth of numerical geometry. We set z_0 which is long enough to neglect the numerical errors caused by the shortages of thermal diffusion length in the model under assumptions of the thermal properties and rotational period (Table 2).

The solar flux is given by

$$F_S(t) = \begin{cases} -S(r)\mathbf{s} \cdot \mathbf{n} & (\mathbf{s} \cdot \mathbf{n} < 0), \\ 0 & (\mathbf{s} \cdot \mathbf{n} \geq 0), \end{cases} \tag{4}$$

where $S(r) = S_0/r^2$ is irradiance at solar distance r and S_0 is solar constant (Table 3); s is a unit vector of solar light, which is determined by the position of the asteroid; \mathbf{n} is the normal vector of a point on the surface whose time evolution is determined by the spin vector of the asteroid.

4 Simulations

4.1 Image Simulation and Rendering Procedure

Utilizing our numerical models described above, we simulated the expected images that will be obtained by the TIR from nominal operation in the global mapping phase. We took into account the geometrical conditions of the spacecraft and the target asteroid, as depicted in Fig. 3 (see Appendix A for mathematical description). As for the observing geometry, we assumed that the distance between the spacecraft and the target asteroid was fixed at 20 km with a space in the sub-earth position (SEP). We applied parallel projection in the rendering process from a 3D to a 2D image. The pixel number of a synthesized image, 328×248 arrays of pixels, is the same as the actual specification of the imaging device. The diameter of the asteroid in an image is expected to be 50 pixels at the target distance of 20 km.

4.2 Effective Temperature in a Pixel

The thermal detector of the TIR is a micro-bolometer with a wavelength of 8 to 12 μm . The temperature in a pixel is obtained as an effective temperature that is the radiatively averaged value of the energy emitted from all the sub-pixels in a pixel of an image. We divided one pixel into 10×10 sub-pixels in the numerical calculations. We assumed thermodynamic equilibrium in each of sub-pixel grid point. The amounts of radiative energy emitted from each sub-pixel are integrated to provide the effective temperature in a pixel, assuming a Lambertian emitter. In this process, artificial noise, which is simulated as random errors of 0.3 K in a pixel of the TIR and the systematic bias of 3 K in each of the TIR images were added to the numerical results.

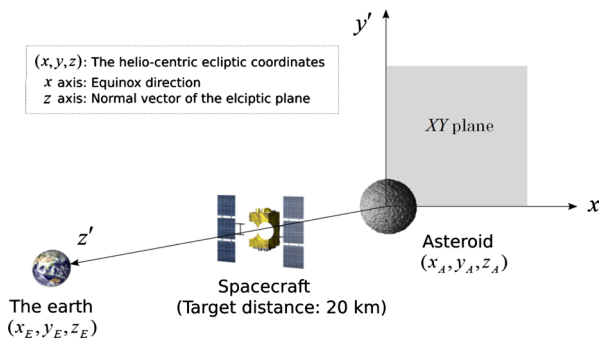


Fig. 3 Definition of the coordinate systems for simulations of the TIR images. The (x, y, z) is the helio-centric ecliptic coordinates. We define asteroid-centric coordinates (x', y', z') as the z' axis is aligned with the asteroid-earth vector and the x' axis is parallel to the xy plane. The y' axis satisfies the right-hand rule. The observer (spacecraft) is on the z' axis with the distance to the asteroid: 20 km. We define XY plane as a rendering plane of the images. The XY plane is originally equivalent to $x'y'$ plane

We calculated the intensity of the component in a pixel as

$$\tilde{E}(u, v) = \frac{1}{100} \sum_{i=0}^9 \sum_{j=0}^9 E(T(X_i^{(u,v)}, Y_j^{(u,v)})), \tag{5}$$

where $T(X_i^{(u,v)}, Y_j^{(u,v)})$ is the temperature of a sub-pixel in a pixel (u, v) ; $0 \leq u \leq 247, 0 \leq v \leq 327$. Thermal energy as a function of temperature $E(T)$ is expressed in Plank’s law of radiation and the function $B(\lambda, T)$:

$$E(T) = \int_{8\mu\text{m}}^{12\mu\text{m}} B(\lambda, T) d\lambda. \tag{6}$$

The intensity of radiation is given by

$$B(\lambda, T) = \frac{2\pi hc_0^2}{\lambda^5} \frac{1}{\exp(\frac{hc_0}{\lambda k_B T}) - 1}, \tag{7}$$

where h is Planck constant, c_0 is speed of light, and k_B is Boltzmann constant (Table 3).

Consequently, we obtain the effective temperature in a pixel using the inverse function of the averaged energy:

$$T(u, v) = E^{-1} \tilde{E}(u, v). \tag{8}$$

In the calculation of Eq. (8) with the inverse function of Eq. (6), we used a lookup table of temperature as a function of radiance, whose implementation was based on Eqs. (6) and (7).

4.3 Fitting Procedure to Examine Uncertainties of Thermal Phase Delay

The diurnal curve of surface temperature is restored by collecting the intensity of the pixel from the images. Data points that are extracted from the images are fitted as a quadratic function using the least square method to determine the fitting coefficients. This procedure is repeated 100 times with different random noise using the same number of simulated images to determine uncertainties of thermal phase delay. The fitting function is given by

$$T = a\phi^2 + b\phi + c \tag{9}$$

where $a, b,$ and c are the coefficients of the polynomial and ϕ is the longitudinal variable of a fitting curve. The longitude of the maximum temperature is given by

$$\phi_m = -\frac{b}{2a}. \tag{10}$$

An example of the fitting results is plotted in Fig. 4. We selected the pixels that were located in the same latitude in a TIR image and fitted them using the fitting function. We determined the latitudinal width of the pickup range to be $\pm 2^\circ$ from the centered latitude in order to retain the number of data points for the fitting method. The longitudinal range of picking up data points is -30° to 60° where the fitting curve is in symmetrical form against the longitude of maximum temperature. The scatter of the points in Fig. 4 results from not only the random errors of the detector, but also the areal (or angular) coverage in a pixel to the asteroid surface. The pixels near the edge of an image have wider areal coverage of the asteroid surface per pixel in latitude and longitude. Thus, the temperatures from a wider area on the surface are mixed compared to that of the pixel near the center of an image.

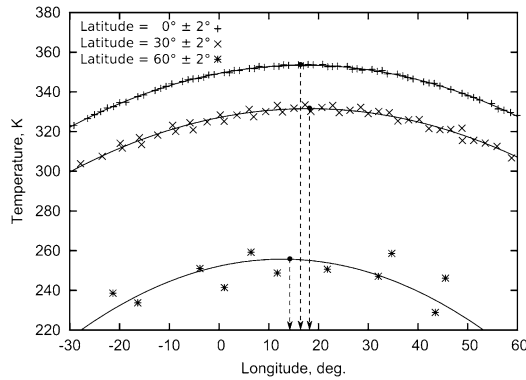


Fig. 4 Schema for illustrating the retrieval of the longitude of maximum temperature using the least square fitted curves. The data points are from pixels of a simulated TIR image. Zero longitude corresponds to sub-solar longitude on the surface of the asteroid. The number of data points in each latitude changes according to the asteroid’s spin vector. In this example, the data is from $\Gamma = 400 \text{ J m}^{-2} \text{ s}^{-1/2} \text{ K}^{-1}$ in the spin vector $(73^\circ, -62^\circ)$ in Aug 1st, 2018. The scatter of the points results from random errors of the detector and the areal coverage of a pixel to the asteroid surface in an image; the centered pixels have higher spatial resolution than those near the edge. Temperature in a pixel is an averaged value of those in sub-pixels

5 Results

Figure 5 shows the longitudinal delay of temperature peak, ϕ_m , and its variance, $\Delta\phi_m$, given from the 100-time fittings for various latitude. The spin vector is assumed to be $(73^\circ, -62^\circ)$. The results show that ϕ_m depends on the thermal inertia. In the case of Aug 1st, 2018 (upper panel of Fig. 5), $\Delta\phi_m$ remains small relative to ϕ_m at almost whole latitude range. Accordingly, we estimate the thermal inertia of surface material with high accuracy in this timing. On the other hand, in the case of May 1st, 2019 (lower panel of Fig. 5), the dependency of ϕ_m on thermal inertia becomes less obvious, especially in the northern hemisphere (lower hemisphere of left bottom figure). Even zero thermal inertia produces an apparent thermal phase delay due to technical reason of numerical fitting to a quadratic curve.

Figure 6 represents the results of the simulations in which the spin vector is assumed to be $(331^\circ, 20^\circ)$. In the case of May 1st, 2019 (upper panel of Fig. 6), the dependency of ϕ_m on the thermal inertia is obvious. However, the large $\Delta\phi_m$ means that the estimation of the thermal inertia of Ryugu’s surface is inaccurate in this timing. On the other hand, in the case of July 1st, 2019 (lower panel of Fig. 6), we can confidently estimate the thermal inertia from the longitudinal delay of temperature peak calculated from Eq. (10).

To clarify the time variation of uncertainties of estimation of the thermal inertia, we calculated averaged $\Delta\phi_m$ s around the SEP that corresponds to sub-satellite point, for various days during the operational period (Fig. 7). Figures 7(a) and 7(b) show the time evolution of the averaged longitudinal delay, $\langle\Delta\phi_m\rangle$ within the latitudinal range $\text{SEP} \pm 4^\circ$, and Figs. 7(c) and 7(d) show $\langle\Delta\phi_m\rangle$ within the latitudinal range of $\text{SEP} \pm 20^\circ$ for various thermal inertia. These figures show the choice of the latitudinal range does not change the tendency of the time evolution of $\langle\Delta\phi_m\rangle$.

The averaged variance of the longitudinal phase delay changes up to one to two orders of magnitude with time. For example, $\langle\Delta\phi_m\rangle$ increases after March 2019 in the case with the spin vector $(73^\circ, -62^\circ)$ (Figs. 7(a) and 7(b)). These time variations are caused by the change of the observable longitude range on the asteroid’s surface from TIR, which will restrict the reproduction of the diurnal profile of surface temperature after March 2019. The

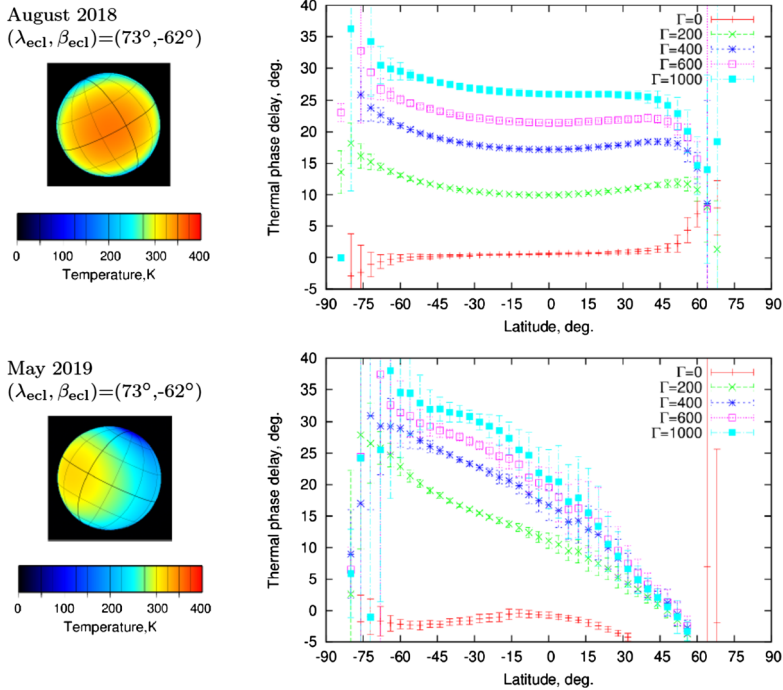


Fig. 5 Examples of simulated images ($\Gamma = 400 \text{ J m}^{-2} \text{ s}^{-1/2} \text{ K}^{-1}$; the *broad lines* correspond to the equator and sub-solar longitude) and results of fitting procedures for $\Delta\phi_m$. The spin vector solution is $(73^\circ, -62^\circ)$, the retrograde type. The *error bars* correspond to 1σ of the fitting iterations, which add the random error of the detector. *Upper panel* (Aug 1st, 2018) shows one of the results in observing opportunities. $\Delta\phi_m$ remains small relative to ϕ_m over a wide range of latitudes. *Lower panel* (May 1st, 2019) shows the result from the inappropriate observing condition. The dependency of ϕ_m on thermal inertia is not clear, especially in the northern hemisphere. The *lines of error bars* and *data points* overlap with each other

observable longitude of the asteroid in a TIR image is geometrically determined by the difference between the longitude of sub-solar point (SSP) and the longitude of SEP on the asteroid because the spacecraft (or the TIR) maintains the position of SEP of Ryugu in this simulations (e.g., Fig. 3). The difference angle is positive when the TIR has a wider coverage of the morning hemisphere of Ryugu's surface, while it is negative when the TIR has a wider coverage of the evening hemisphere. Because we use the diurnal thermal delay to estimate thermal inertia in this study, it is preferred that the TIR monitors a wider area of the evening hemisphere. Accordingly, the longitudinal difference is a useful index in determining the appropriate timing for observing thermal inertia in remote sensing. Figure 7(e) represents the longitude difference for the case with spin vector $(73^\circ, -62^\circ)$.

In contrast, when the asteroid has the horizontal spin vector $(331^\circ, 20^\circ)$, the latitude of the sub-solar point is also the critical parameter as well as the difference angle between the SSP and SEP longitudes (Figs. 7(b), 7(d) and 7(f)). When the sub-solar point comes into the polar region of Ryugu, the surface of the asteroid is illuminated from almost the same illumination angle. Consequently, the temperature distribution over the surface is averaged in the longitudinal direction, and the thermal phase delay becomes faint over the surface, regardless of the degree of thermal inertia. For this reason, the reproducibility of the diurnal curves for thermal inertia using the quadratic fitting method will be lowered during the

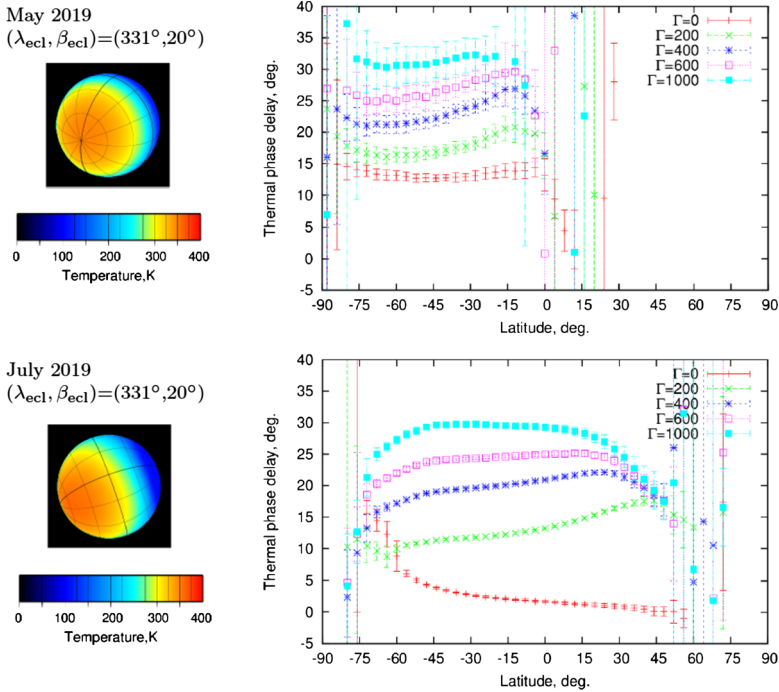


Fig. 6 Examples of simulated images ($\Gamma = 400 \text{ J m}^{-2} \text{ s}^{-1/2} \text{ K}^{-1}$; the *broad lines* correspond to the equator and sub-solar longitude) and results of fitting procedures for $\Delta\phi_m$. The spin vector solution is $(331^\circ, 20^\circ)$, the horizontal type. The *error bars* correspond to 1σ of the fitting iterations, which add the random error of the detector. *Upper panel* (May 1st, 2019) shows the result of the inappropriate observing condition. When the sub-solar point comes into the polar region, the temperature distribution over the surface is averaged in the longitudinal direction, and the thermal phase delay becomes faint over the surface. *Lower panel* (Jul 1st, 2019) shows one of the observing opportunities. $\Delta\phi_m$ remains small relative to ϕ_m over a wide range of latitudes

periods of higher sub-solar latitudes. In fact, this situation can happen in the TIR observation in Hayabusa2 when the target asteroid has horizontal spin vector tilting toward the ecliptic plane. The spin vector $(331^\circ, 20^\circ)$ is one of the cases: the top figure in Fig. 6 depicts a typical example.

Additionally, we note here that the fitting errors could be reduced to some extent if we adjust the longitudinal range of the fitting data (e.g. Fig. 4) or change the fitting functions to other types of polynomial expressions (e.g., sinusoidal curves, instead of using the quadratic curves) to measure the diurnal phase delay. This is out of scope in this study.

6 Discussion

6.1 Accuracy of Thermal Inertia and Observation Opportunity in the Ideal Case

We evaluate uncertainties of thermal inertia in the ideal case using

$$\Delta\Gamma = \left| \frac{d\Gamma}{d\phi_m} \right| \Delta\phi_m, \tag{11}$$

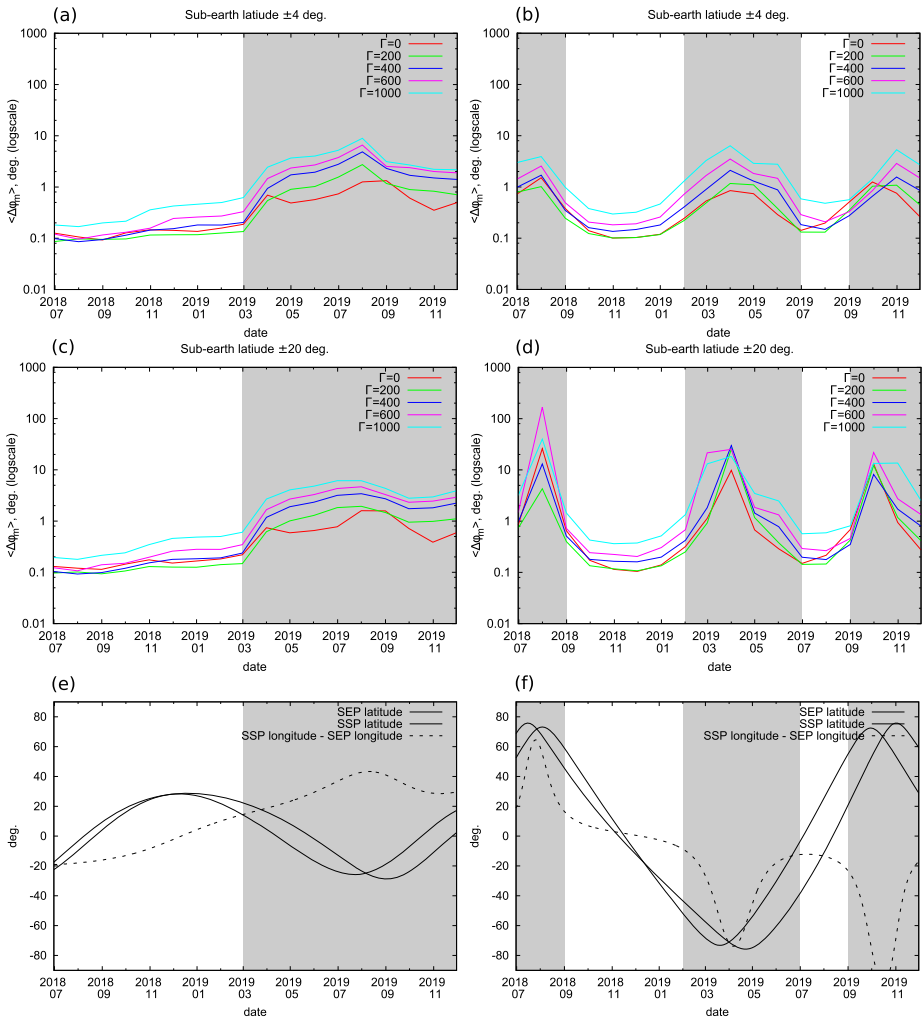


Fig. 7 (a)–(d) Averaged uncertainties of thermal phase delay ($\langle \Delta\phi_m \rangle$) in the latitudinal ranges from July 2018 to December 2019: (a), (b) SSP $\pm 4^\circ$; (c), (d) SSP $\pm 20^\circ$; (e), (f) curves of SEP and SSP latitudes of Ryugu are shown. The curves of the difference angle between the longitudes of SSP and SEP are also shown here. When the difference angle is positive, the TIR has narrower coverages of the evening sphere of Ryugu’s surface; The spin vector is $(73^\circ, -62^\circ)$ in (a), (c), and (e); $(331^\circ, 20^\circ)$ in (b), (d), and (f); The gray fields show the timings that $\langle \Delta\phi_m \rangle$ is greater than 1 degree. The timings in the white fields will be appropriate seasons to measure the thermal inertia of Ryugu using the TIR

where $\Delta\phi_m$ is the estimated uncertainty of the diurnal phase delay of the surface temperature. Here, $\Delta\phi_m$ could be decreased to less than 1 degree under an observation opportunity, based on the result of the imaging simulations (Fig. 7). The error of thermal inertia $\Delta\Gamma/\Gamma$ in the observation opportunity will be less than 20% when Γ is below $1000 \text{ J m}^{-2} \text{ s}^{-1/2} \text{ K}^{-1}$.

The opportunity for observing thermal inertia in the spin vector $(73^\circ, -62^\circ)$ is described from the difference angle between the longitudes of SSP and SEP; $|\phi_{\text{SSP}} - \phi_{\text{SEP}}| < 20^\circ$. This condition will last from July 2018 to March 2019 (Fig. 7(e)). In contrast, the observation opportunity for the horizontal spin vector $(331^\circ, 20^\circ)$ is described from the sub-solar latitude;

$-40^\circ < \theta_{SSP} < 40^\circ$, where we considered the problem caused by the high latitude of SSP in the previous chapter and excluded these timings. The appropriate condition comes around from September 2018 to February 2019 and from July to September 2019, which will be the observation opportunity for the operation of the TIR in remote sensing. The difference angle in the longitude of SSP and SEP is still important in this case: we excluded the timing from September to October 2019 because the difference angle was over 20° (smaller than -20°) though the SSP latitude was smaller than 40° (Fig. 7(f)).

While the result from the ideal case is important for preparing for scientific observations and mission operations, the lack of surface roughness in thermal modeling is oversimplification. Errors of thermal inertia will be significantly influenced by this effect. Local topography or surface roughness will be essential in thermal modeling of a realistic asteroid surface. We performed a preliminary study on this issue, which will be described in Sect. 6.3.

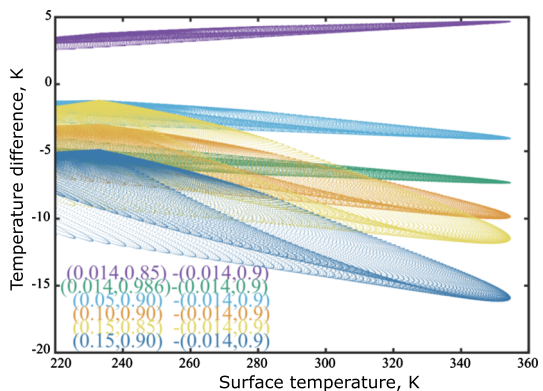
6.2 Estimation of Albedo and Emissivity from Regression Analysis

The energy balance at the surface is given in Eq. (2). In general, the amount of conductive heat flow toward the ground is much smaller than the energy influx via solar irradiation. Neglecting the internal heat flux, we obtain quasi-steady surface temperature from $T \sim \sqrt[4]{(1-A)F/\epsilon\sigma}$, which means the surface temperature is determined by the ratio $(1-A)/\epsilon$ under constant solar flux F . Here, the albedo is difficult to determine independently of emissivity. However, the surface temperature profile in fact depends on thermal inertia, which indicates that the heat flux from the ground also affects the surface temperature profile. From this perspective, albedo and emissivity can be separated and estimated independently.

We carried out numerical tests of surface temperature using various values of albedo and emissivity to evaluate the effect of these parameters on surface temperature. Figure 8 depicts the correspondence of albedo and emissivity with surface temperature. Thermal inertia is assumed to be $400 \text{ J m}^{-2} \text{ s}^{-1/2} \text{ K}^{-1}$ in this calculation. Higher surface temperature is achieved with lower albedo and lower emissivity, whereas lower surface temperature is achieved with higher albedo and higher emissivity. We confirmed that the absolute surface temperature was not always the same even if the same amount of $(1-A)/\epsilon$ was assumed with finite thermal inertia.

For detailed analysis of the dependence of surface temperature on albedo and emissivity, we focused on the temperature profile at the equator. Thermal profiles with various values of albedo and emissivity are fitted by a quadratic function, as discussed in the previous

Fig. 8 Schema for illustrating that temperature distribution is not always the same even if the same amount of $(1-A)/\epsilon$ is assumed with finite thermal inertia. Difference in surface temperature modeled with various (A, ϵ) from the nominal case $(A = 0.014, \epsilon = 0.9)$; $(0.014, 0.85)$, $(0.014, 0.986)$, $(0.05, 0.9)$, $(0.1, 0.9)$, $(0.15, 0.85)$, $(0.15, 0.9)$



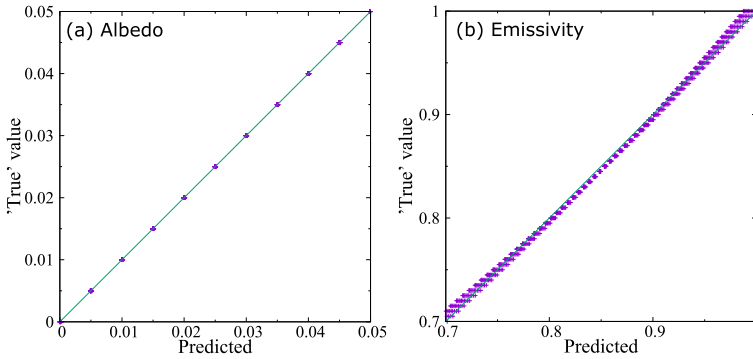


Fig. 9 Uncertainties of the regression functions. **(a)** Bond albedo, Eq. (12); **(b)** Thermal emissivity, Eq. (13)

chapter (Eq. (9)). The ratio $-b/2a$ could change with albedo and emissivity; however, the difference is less than 10% over the entire parameter range in this study. The likely errors of these parameters are less than several percent. This result seems to be due to our simple fitting of quadratic polynomials to sinusoidal curves. Figure 9 plots the relationship between A (and ϵ) and the coefficients obtained by simple linear regression analysis. The resultant sets of coefficients are compiled in Eqs. (12) and (13):

$$A \sim 146.105a + 4.220b - 0.005c + 1.162, \tag{12}$$

$$\epsilon \sim 64.275a - 19.744b + 0.028c + 2.148. \tag{13}$$

Figure 9 implies that we can estimate albedo and emissivity simultaneously, with accuracy exceeding 95%. We demonstrated the estimation of albedo and emissivity for a specific case (in the spin vector $(73^\circ, -62^\circ)$ on August 2018 at the equator); however, this method can be applied to other conditions.

When we consider surface roughness using this approach, the determination of albedo and emissivity would be more uncertain than the ideal case of a smooth surface. The uncertainties of these quantities might be significant, since they are based on the absolute value of temperature itself, contrary to the determination of thermal inertia through the phase shift, which is derived from only the profiles of diurnal temperature.

6.3 A Study on Realistic Rough Surface

6.3.1 TPM with Local Topography and Surface Roughness

In the preceding chapters, we ignored surface topography and surface roughness of the asteroid in thermal modeling. However, we will encounter these problems when performing observations from a close position in remote sensing. In this section, we present our preliminary results of a study on the effect of surface topography on thermophysical estimation using artificial shape models with random rough surfaces. Here, we distinguished surface topography from surface roughness, where surface roughness means the spatially unresolved scale of roughness, which is not explicitly expressed in the surface mesh of the global shape model.

For the numerical approach using TPM, we produced rough surface models by deforming a spherical surface mesh (Fig. 10). The radius of the original sphere is 450 m; the number of vertices of the surface is 2562, and the number of facets is 5120. The spatial resolution

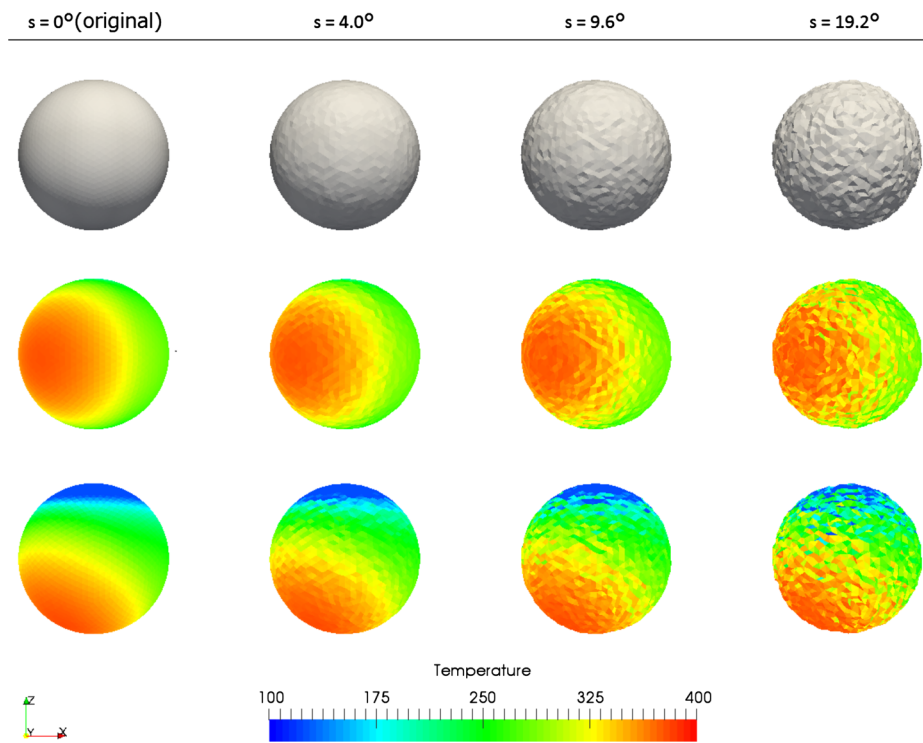


Fig. 10 Surface meshes of rough surface models and examples of global temperature distributions over the surface. The *four figures in the top row* depict the global shapes of surface topographies. The spatial resolution of each facet is 22 m in the smooth sphere. The rough scales of the surface meshes are expressed in the RMS surface slope s (above the top figures). The *four figures in the middle row* are from the spin vector $(73^\circ, -62^\circ)$, and the *bottom four figures* are from $(331^\circ, 20^\circ)$. Thermal inertia is $400 \text{ J m}^{-2} \text{ s}^{-1/2} \text{ K}^{-1}$. These images are not the simulated ones that will be seen from the spacecraft in the rendezvous phase. These figures are represented in the xz plane at a rotational phase. The orientation of the z axis corresponds to that of the spin vector

of the surface facet is 22 m, which is comparable to that of a pixel in a TIR image taken at a target distance of 20 km. We used the software MeshLab (<http://meshlab.sourceforge.net/>) to add artificial random displacement of the surface vertex of the original sphere. We set the input parameters of the maximum displacement of the vertices to 2 m, 5 m, and 10 m.

We calculated RMS surface slope s (Spencer 1990; Davidsson et al. 2015) as a parameter to express the level of rough scale of the topography. The definition of s is given by

$$s = \sqrt{\frac{\sum_{i=1}^N \theta_i^2 b_i \cos \theta_i}{\sum_{i=1}^N b_i \cos \theta_i}}, \tag{14}$$

where N is the total number of the facets in the surface mesh and each of the facts is locally smooth. b_i is the area of a facet i and θ_i is an angle which is made by the normal vector of the facet i and the standard normal of the terrain. We calculated θ_i as

$$\theta_i = \cos^{-1} \mathbf{n}_i \cdot \bar{\mathbf{n}}_i, \quad (15)$$

where \mathbf{n}_i is a facet normal of the rough mesh, and $\bar{\mathbf{n}}_i$ is a normal vector of the original spherical mesh which determines the standard for the facet angle. The values of s are 0° , 4.0° , 9.6° , and 19.2° in the original (smooth), 2 m, 5 m, and 10 m meshes, respectively.

The thermophysical properties are basically the same as the ones described in Sect. 3, except for the use of numerical surface meshes. Additionally, we considered the effect of surface roughness on surface temperature as a function that changes only the effective emissivity of the asteroid surface, following the works of Davidsson et al. (2009) and Leyrat et al. (2011). Since the surface roughness of asteroid Ryugu has not yet been explicitly determined, we adopted the effective infrared emissivity $\varepsilon_{\text{eff}} = 0.73$, which is the observed value of asteroid Steins (Leyrat et al. 2011). The effective emissivity is given by

$$\varepsilon_{\text{eff}} = (1 - \varepsilon\xi)\varepsilon, \quad (16)$$

where ξ is a parameter for surface roughness (which can be derived from lope angle of surface roughness, Hapke 1984), $\xi = 0.2$ for Steins (Leyrat et al. 2011). This approach does not explicitly consider mutual energy exchanges by radiation or local shadowing between the surface facets.

6.3.2 Effect of Rough Surface on the Thermal Phase Delay

We fitted the surface temperatures that were generated by the rough surface models to determine whether the thermal phase delay can still be retrieved under rough surface topographies. Two types of spin vectors are also considered in this study. This time, we picked only the surface temperatures on the equatorial zone under the appropriate seasons for thermal observations (Aug 2018 and July 2019), as discussed in the previous chapter. Quadratic least-square fitting is applied to the data of latitude 0 ± 2 degrees. The fitting longitudinal range is -30 to 60 degrees against the sub-solar longitude. Figure 11 depicts the profiles of surface temperatures from the four models of different rough scales with the same thermal inertia in one graph. The sub-solar longitude is at 0 degree in these graphs.

We evaluated uncertainties in the estimation of the phase delay using least square fittings based on a series of data generated in the diurnal motion. A data set contains 360 data files that are sampled in a rotation and contain the surface temperature of the entire facets. We produced data set using each of the four rough surfaces in TPM with parameters of thermal inertia 200, 400, and $600 \text{ J m}^{-2} \text{ s}^{-1/2} \text{ K}^{-1}$. We repeated the fitting procedures using each of the data files to calculate the fitting coefficient (a and b in Eq. (10)) and integrated these results to calculate the average value and standard deviation of the fitting results to determine the amount of thermal phase shift. The error bars in Figs. 12(a) and (b) correspond to 1σ from these results.

6.3.3 Accuracy of Thermal Inertia in Rough Surfaces

We found that the feasibility of thermal inertia from the diurnal phase delay depended greatly on the orientation of the spin vector. The thermal phase delay could be determined without being strongly affected by local topography if the target asteroid has the spin vector ($73^\circ, -62^\circ$) within the range of the rough scales in this study. In contrast, we presume that estimation of thermal inertia might not be feasible for the spin vector orientation ($331^\circ, 20^\circ$) when we consider the likely surface topography of the NEAs, which will be rough in several meters of the vertical scale towards the horizontal scale of 20 m, like asteroid Itokawa.

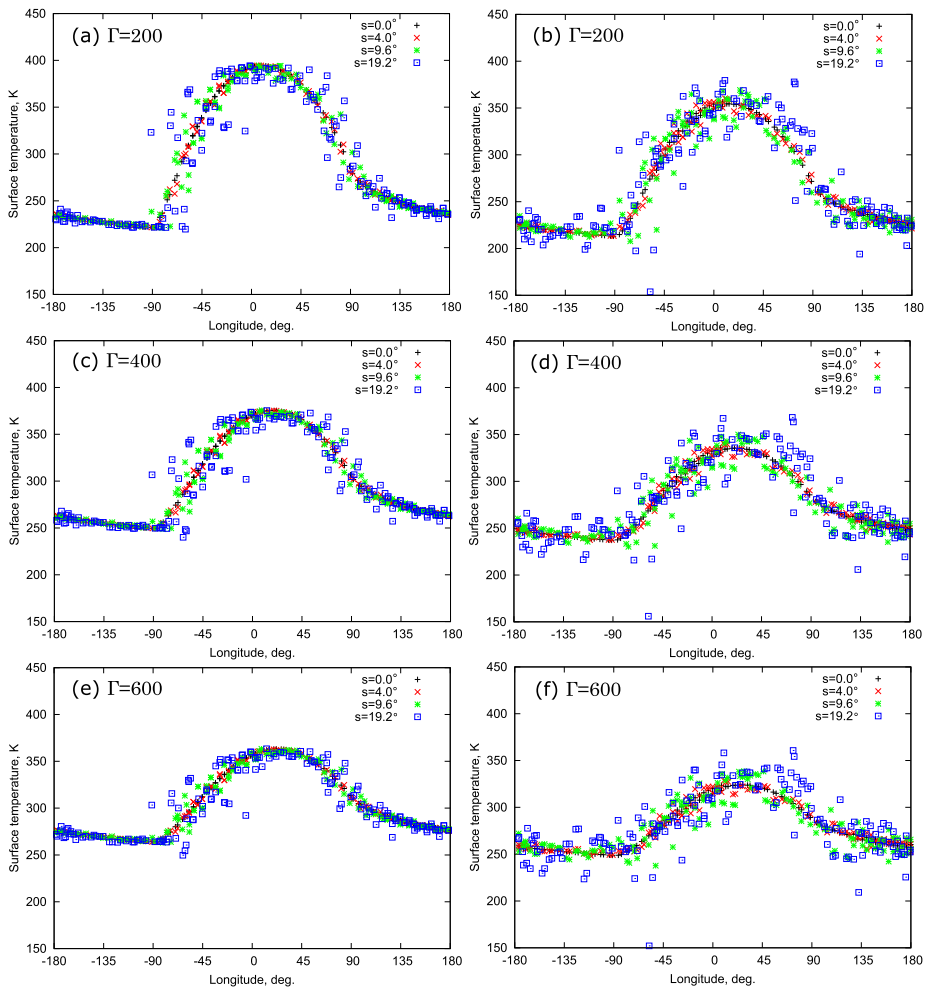


Fig. 11 Temperature profiles of the rough surface models in a diurnal motion. (a), (c), (e) Spin vector $(73^\circ, -62^\circ)$ in August 2018; (b), (d), (f) Spin vector $(331^\circ, 20^\circ)$ in July 2019. Thermal inertia is $200 \text{ J m}^{-2} \text{ s}^{-1/2} \text{ K}^{-1}$ in (a), (b); 400 in (c), (d); and 600 in (e), (f). The temperature data are selected from the equatorial zone. Surface roughness is also included through the self-heating parameter, which controls the effective thermal emissivity ($\epsilon_{\text{eff}} = 0.73; \xi = 0.2$)

Considering the errors of phase shift of Fig. 12 to be combined with the results of the ideal case, uncertainty of thermal inertia will be greater than 50% if the rough scale is $s = 9.6^\circ$ (vertically 5 m towards the horizontal scale of 20 m) in the spin vector $(73^\circ, -62^\circ)$. The same extent of roughness could result in errors exceeding 200% in the spin vector $(331^\circ, 20^\circ)$. Thermophysical estimation is likely to be difficult in the horizontal vector $(331^\circ, 20^\circ)$, while determination of the diurnal phase delay in the spin vector $(73^\circ, -62^\circ)$ will still be feasible unless the target asteroid has a significantly rough topography.

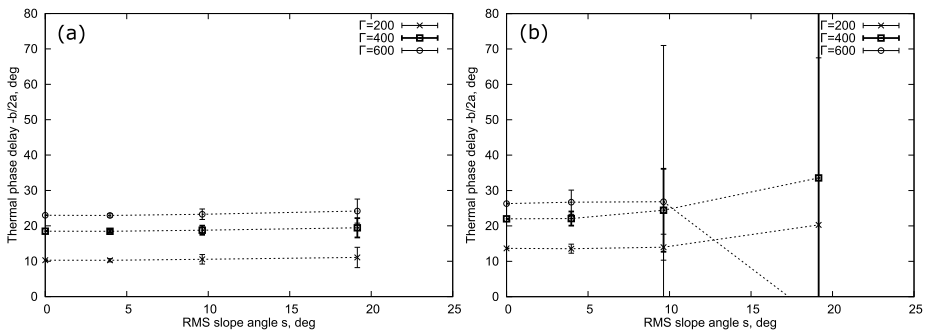


Fig. 12 Estimated thermal phase delay using the rough surface models from the quadric least square fittings. **(a)** Spin vector (73° , -62°) in August 2018; **(b)** spin vector (331° , 20°) in July 2019; The feasibility to accurately determine the thermal phase delay is strongly affected by the combination of surface topographies and directions of spin vector, which will change illumination conditions on the surface. The fitting procedure for the phase estimations fails when the surface slope angle exceeds 10° in the spin vector (331° , 20°)

6.4 Crucial TIR Observations and Data to Distinguish Roughness Effects from Thermal Inertia Effects

There is a degeneracy between roughness and thermal inertia in the thermal effects on temperature in disc-integrated data and it is difficult to disentangle the effects of these parameters. In disk-resolved data, retrieval of temperature depends strongly on illumination and observation geometry (e.g., Rozitis and Green 2011). Indeed, we can find the strong dependencies in our study in Sect. 6.3 (Fig. 11) when we consider the results from different spin vectors as the results from different illumination conditions. Therefore, it is important to observe a specific surface region at the observing condition that the effects of surface roughness are as small as possible in order to derive the thermal inertia.

Numerical studies with various types of roughness models (e.g., concave spherical segment; parallel sinusoidal trenches; random Gaussians) provides a practical advice that the nadir observations (emergence angle = 0°) of regions near the sub-solar point with smaller incidence angle ($< 30^\circ$) will be suited to the derivation of thermal inertia from dayside emission near the Planck curve peak at 1 AU (Davidsson et al. 2015). Inversely, when we are interested in the information about surface roughness, the regions illuminated at high incidence will be crucial to determine the level of roughness.

We planned preliminary strategies about how we should operate spacecraft and onboard instruments in the Hayabusa2 mission to obtain the data that will allow us to clearly determine thermal inertia and surface roughness. One of the straight forward approaches is to observe a specific region on Ryugu's surface at various illumination and viewing conditions and collect the data which have different sensitivities to surface roughness. These data will be able to assist TPM analyses. Also, we considered observations to the locations at dawn and dusk on the asteroid surface. In these moments, the surface temperature will less disturbed by rough surfaces under an appropriate viewing condition (e.g., Fig. 11).

The information about surface roughness can be obtained using data from other devices on board the spacecraft (e.g., the optical camera (ONC) and the laser altimeter (LIDAR)). The high resolution optical images of asteroid surface (e.g., images that will be obtained in close observations such as the touch down operations for sample acquisitions) will allow us to directly investigate the roughness of Ryugu's surface.

Moreover, the Hayabusa2 spacecraft carries a lander (MASCOTT) with a radiometer (MARA) which uses thermopile sensors with 4 bandpass channels and can measure brightness temperature in mid-infrared wavelength similar to the TIR (Grott et al. 2015, this issue). The MARA will measure at least a whole diurnal temperature on Ryugu's surface. The in-situ measurement as a time series at a single site on asteroid surface will provide valuable data for interpretation of the thermal infrared data from the global remote sensing.

We are now planning to perform several optional operations of spacecraft to cover wide range of observing conditions to obtain the crucial data for the disentanglement of thermal inertia and surface roughness. Though the spacecraft is basically fixed to the sub-earth direction as described before, the new operational plan will include several attempts to change the spacecraft direction toward the asteroid or move the spacecraft from the nominal position to achieve multi illumination and viewing conditions.

7 Summary and Conclusions

We simulated images of the target asteroid seen from the thermal infrared imager (TIR) onboard Hayabusa2 in the proximity phase from July 2018 to December 2019 using numerical calculations. The implementations are based on the TPM and the specification of the TIR to detect radiation emitted from the asteroid. We considered a realistic observing geometry of the spacecraft using the orbital position of the asteroid as well as the spin pole orientations. Although ground-based observation prefers the retrograde rotation of spin vector (73° , -62°) to the type (331° , 20°), we adopted both solutions to study the effect of spin pole in the thermophysical observations. We studied the feasibility of the observation using an ideal body with a smooth and spherical surface to prepare for mission operations and thermophysical estimations. While we basically assumed a smooth surface in this study, it is true that surface roughness can cause significant errors in thermophysical estimation for the ideal case. We also included a discussion about this problem in a preliminary study, which will be a basis for the next step of our future work.

Considering dayside observation of the target asteroid in remote sensing, we selected a method to determine the thermal inertia from the phase delay of diurnal temperature profiles. Here, thermal inertia can be estimated independently of albedo and emissivity. Moreover, the use of temperature near the sub-solar region will be appropriate to avoid non-Lambertian emitters at high solar phase angles. Simultaneous estimation of albedo and thermal emissivity is also feasible with known thermal inertia after determination through the thermal phase delay, which will be our primary strategy for estimating thermophysical properties.

Appropriate conditions for observing Ryugu using the TIR significantly change according to the spin vector solutions of the target asteroid. In a spin vector of $(\lambda_{\text{ecl}}, \beta_{\text{ecl}}) = (73^\circ, -62^\circ)$, an opportunity to monitor the thermal phase delay is the condition less than 20° in the difference angle between the longitudes of SSP and SEP. From the arrival of the Hayabusa2 spacecraft in mid-2018, this condition will last until March 2019. In a spin vector of $(331^\circ, 20^\circ)$, the season when not only the difference angle between the longitudes of SSP and SEP is less than 20° but also the sub-solar latitude comes between -40° and 40° (September 2018 to February 2019, and July to September 2019) will be the observation opportunity.

We evaluated the uncertainty of thermal inertia observed at a target distance of 20 km using the TIR in the operational period. The uncertainty was less than 20% under the appropriate timings based on our numerical simulations if the surface was smooth. Uncertainties of bond albedo and thermal emissivity are expected to be less than 5% within the likely

range of these values based on regression analysis. We note here the significant uncertainties in some of these results, due to ignoring surface roughness in the thermal modeling. When we consider the rough surfaces of the asteroids, uncertainty could exceed 50% at a realistic rough scale. Determination of thermal inertia will be more difficult if the asteroid has a spin vector of $(331^\circ, 20^\circ)$.

The solution of the spin vector of the target asteroid is very important for thermophysical estimation of asteroid surfaces using remote sensing instruments, which will also be informative for ground-based observations of asteroids at thermal infrared wavelengths (e.g., Müller et al. 2014). The Hayabusa2 will allow us to make a better understanding of thermophysical properties of a primitive asteroid from the in-situ investigations, and also helping us better interpret of spatially-integrated thermal infrared data acquired by the ground based facilities.

8 Future Work

Although we approximated the shape of Ryugu as a perfect spherical body in this study, we must include more practical problems like surface topography or surface roughness and thermal infrared beaming when we reproduce images of the target asteroid using scientific computations. Shadowing on the surface and reabsorption of radiated thermal energy are expected to be necessary in simulating local temperature variations. Moreover, 3D heat conduction might be essential for explicit disentanglement of thermal inertia and surface roughness for NEAs with high thermal inertia (Davidsson and Rickman 2014). In addition, the temperature dependence of thermal inertia and non-Lambertian emitters are important for handling more realistic surfaces (Groussin et al. 2013; Keihm et al. 2012, 2015).

While we started work on surface roughness in the preliminary study using some rough surface meshes in this study, future work will interpolate a more realistic approach and the value of surface roughness for Ryugu in thermal modeling. Reproduction of a detailed surface temperature map is also important for spectroscopy, since thermal emission could disturb the intrinsic spectrum of surface materials and its interpretations. The thermal model is helpful in removing the thermal continuum flux from the data in the mid-infrared region (Emery et al. 1998).

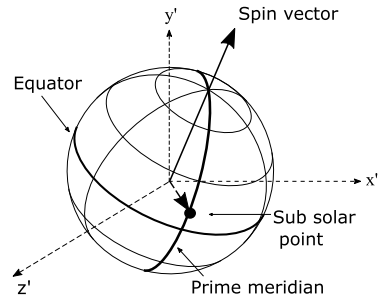
Ongoing studies of existing and future optical and thermal observations will probably constrain the spin vector, thermal inertia, size, shape, and albedo considerably. This TIR study can be updated well before the start of Hayabusa2 proximity operations on asteroid Ryugu.

Acknowledgements We would like to thank the two anonymous reviewers whose comments and suggestions helped improve this manuscript. We also thank Sunao Hasegawa for helpful discussion of this work about thermal modelings.

Appendix A: Mathematical Description of the Imaging Simulation

We now describe mathematical implementations for simulating TIR images. In this procedure, we calculated the components of the spin vector in the imaging coordinate system to determine the asteroid's local equatorial longitude and latitude, which are combined with the reference point of the sub-solar point.

Fig. 13 Definition of the prime meridian in the imaging coordinate system



The base vectors of the imaging coordinate system (x', y', z') are defined based on the heliocentric ecliptic coordinates of the asteroid (x_A, y_A, z_A) and the earth (x_E, y_E, z_E) , which are given by (see Fig. 3)

$$e'_z = \begin{bmatrix} (x_E - x_A)/|EA| \\ (y_E - y_A)/|EA| \\ (z_E - z_A)/|EA| \end{bmatrix}, \tag{17}$$

$$e'_x = \begin{bmatrix} -(y_E - y_A)/|EA'| \\ (x_E - x_A)/|EA'| \\ 0 \end{bmatrix}, \tag{18}$$

$$e'_y = e'_z \times e'_x, \tag{19}$$

where

$$|EA| = \sqrt{(x_E - x_A)^2 + (y_E - y_A)^2 + (z_E - z_A)^2}, \tag{20}$$

$$|EA'| = \sqrt{(y_E - y_A)^2 + (x_E - x_A)^2}. \tag{21}$$

The spin vector of the asteroid in the imaging coordinates is given by

$$spin' = (spin \cdot e'_x)e'_x + (spin \cdot e'_y)e'_y + (spin \cdot e'_z)e'_z, \tag{22}$$

where

$$spin = \begin{bmatrix} \cos \beta_{ecl} \cos \lambda_{ecl} \\ \cos \beta_{ecl} \sin \lambda_{ecl} \\ \sin \beta_{ecl} \end{bmatrix}. \tag{23}$$

We obtain the components of spin vector in the imaging coordinate system:

$$\lambda'_{ecl} = \tan^{-1} \frac{spin'_z}{spin'_x}, \tag{24}$$

$$\beta'_{ecl} = \tan^{-1} \frac{\sqrt{(spin'_x)^2 + (spin'_z)^2}}{spin'_y}. \tag{25}$$

The longitude of the prime meridian is defined so as to coincide with the sub-solar longitude in the asteroid-centric coordinate system (Fig. 13). Sub-solar longitude and latitude are defined as follows, including the orbital position of a planet:

$$\phi'_{SSP} = \tan^{-1} \frac{ssp'_z}{ssp'_x}, \tag{26}$$

$$\theta'_{SSP} = \tan^{-1} \frac{\sqrt{(ssp'_x)^2 + (ssp'_z)^2}}{ssp'_y}, \tag{27}$$

where the sub-solar vector expressed in (x', y', z') system is

$$ssp' = (ssp \cdot e'_x)e'_x + (ssp \cdot e'_y)e'_y + (ssp \cdot e'_z)e'_z \tag{28}$$

and the normalized vector of sub-solar point expressed in (x, y, z) system is

$$ssp = \begin{bmatrix} -x_A/r \\ -y_A/r \\ -z_A/r \end{bmatrix}, \tag{29}$$

where

$$r = \sqrt{x_A^2 + y_A^2 + z_A^2}. \tag{30}$$

The view seen from the direction of the spacecraft camera is made by projecting the 3D coordinates of asteroid in (x', y', z') to a rendering plane $x'y'$. We redefine the $x'y'$ plane as a XY plane for simple representation of symbols.

The 2D components are given by

$$\begin{bmatrix} X \\ Y \end{bmatrix} = \begin{bmatrix} 1 & 0 & 0 \\ 0 & 1 & 0 \end{bmatrix} \begin{bmatrix} x' \\ y' \\ z' \end{bmatrix}, \quad z' \geq 0 \tag{31}$$

$$\begin{bmatrix} x' \\ y' \\ z' \end{bmatrix} = \begin{bmatrix} R \sin \theta' \cos \phi' \\ R \cos \theta' \\ R \sin \theta' \sin \phi' \end{bmatrix} \equiv R \mathbf{vec}(\theta', \phi') \tag{32}$$

where R is the radius of the target asteroid.

The asteroid-centric equatorial latitude Θ and longitude Φ at (X, Y) , where $X^2 + Y^2 < R^2$ is satisfied in the image coordinate, are calculated based on the definition of the projected plane in imaging coordinates and the radius of the target asteroid:

$$\Theta = \frac{\pi}{2} - \cos^{-1}(\mathbf{p} \cdot \mathbf{q}), \tag{33}$$

$$\Phi = \begin{cases} \cos^{-1} \frac{(\mathbf{p} \times \mathbf{s}) \cdot (\mathbf{p} \times \mathbf{q})}{|\mathbf{p} \times \mathbf{s}| |\mathbf{p} \times \mathbf{q}|} & \text{for } (\mathbf{p} \times \mathbf{s}) \cdot \mathbf{q} \geq 0, \\ -\cos^{-1} \frac{(\mathbf{p} \times \mathbf{s}) \cdot (\mathbf{p} \times \mathbf{q})}{|\mathbf{p} \times \mathbf{s}| |\mathbf{p} \times \mathbf{q}|} & \text{for } (\mathbf{p} \times \mathbf{s}) \cdot \mathbf{q} < 0, \end{cases} \tag{34}$$

where

$$\mathbf{p} = \mathbf{vec}(\beta'_{\text{ecl}}, \lambda'_{\text{ecl}}), \tag{35}$$

$$\mathbf{s} = \mathbf{vec}(\theta'_{\text{SSP}}, \phi'_{\text{SSP}}) \tag{36}$$

and

$$\mathbf{q} = \frac{1}{R} \begin{bmatrix} X \\ Y \\ \sqrt{R^2 - X^2 - Y^2} \end{bmatrix}. \tag{37}$$

References

M. Abe, K. Kawakami, S. Hasegawa, D. Kuroda, M. Yoshikawa, T. Kasuga, K. Kitazato, Y. Sarugaku, D. Kinoshita, S. Miyasaka, S. Urakawa, S. Okumura, Y. Takagi, N. Takato, T. Fujiyoshi, H. Terada, T. Wada, Y. Ita, F. Vilas, P. Weissman, Y. Choi, S. Larson, S. Bus, T. Müller, Ground-based observational campaign for asteroid 162173 1999 JU3. 37th COSPAR Scientific Assembly, Committee on Space Research B04-0061-08 (2008)

- J. Audouard, F. Poulet, M. Vincendon, J.-P. Bibring, F. Forget, Y. Langevin, B. Gondet, Mars surface thermal inertia and heterogeneities from OMEGA/MEX. *Icarus* **233**(0), 194–213 (2014). doi:[10.1016/j.icarus.2014.01.045](https://doi.org/10.1016/j.icarus.2014.01.045)
- A.M. Baldridge, S.J. Hook, C.I. Grove, G. Rivera, The ASTER spectral library version 2.0. *Remote Sens. Environ.* **113**(4), 711–715 (2009). doi:[10.1016/j.rse.2008.11.007](https://doi.org/10.1016/j.rse.2008.11.007)
- J.L. Bandfield, R.R. Ghent, A.R. Vasavada, D.A. Paige, S.J. Lawrence, M.S. Robinson, Lunar surface rock abundance and regolith fines temperatures derived from LRO diviner radiometer data. *J. Geophys. Res.* **116**(E12), E00H02 (2011). doi:[10.1029/2011JE003866](https://doi.org/10.1029/2011JE003866)
- H. Campins, J.P. Emery, M. Kelley, Y. Fernández, J. Licandro, M. Delbó, A. Barucci, E. Dotto, Spitzer observations of spacecraft target 162173 (1999 JU3). *Astron. Astrophys.* **503**(2), 17–20 (2009). doi:[10.1051/0004-6361/200912374](https://doi.org/10.1051/0004-6361/200912374)
- H. Campins, J. de León, A. Morbidelli, J. Licandro, J. Gayon-Markt, M. Delbó, P. Michel, The origin of asteroid 162173 (1999 JU3). *Astron. J.* **146**(2), 26 (2013). <http://stacks.iop.org/1538-3881/146/i=2/a=26>
- M.T. Capria, F. Tosi, M.C. De Sanctis, F. Capaccioni, E. Ammannito, A. Frigeri, F. Zambon, S. Fonte, E. Palomba, D. Turrini, T.N. Titus, S.E. Schrder, M. Toplis, J.-Y. Li, J.-P. Combe, C.A. Raymond, C.T. Russell, Vesta surface thermal properties map. *Geophys. Res. Lett.* **41**(5), 1438–1443 (2014). doi:[10.1002/2013GL059026](https://doi.org/10.1002/2013GL059026)
- S.R. Chesley, S.J. Ostro, D. Vokrouhlický, D. Čapek, J.D. Giorgini, M.C. Nolan, J.-L. Margot, A.A. Hine, L.A.M. Benner, A.B. Chamberlin, Direct detection of the Yarkovsky effect by radar ranging to asteroid 6489 Golevka. *Science* **302**(5651), 1739–1742 (2003). doi:[10.1126/science.1091452](https://doi.org/10.1126/science.1091452)
- A. Coradini, F. Capaccioni, S. Erard, G. Arnold, M.C. De Sanctis, G. Filacchione, F. Tosi, M.A. Barucci, M.T. Capria, E. Ammannito, D. Grassi, G. Piccioni, S. Giuppi, G. Bellucci, J. Benkhoff, J.P. Bibring, A. Blanco, M. Blecka, D. Bockelee-Morvan, F. Carraro, R. Carlson, U. Carsenty, P. Ceroni, L. Colanageli, M. Combes, M. Combi, J. Crovisier, P. Drossart, E.T. Encrenaz, C. Federico, U. Fink, S. Fonti, L. Giacomini, W.H. Ip, R. Jaumann, E. Kuehrt, Y. Langevin, G. Magni, T. McCord, V. Mennella, S. Mottola, G. Neukum, V. Orofino, P. Palumbo, U. Schade, B. Schmitt, F. Taylor, D. Tiphene, G. Tozzi, The surface composition and temperature of asteroid 21 Lutetia as observed by ROSSETA/VIRTIS. *Science* **334**(6055), 492–494 (2011). doi:[10.1126/science.1204062](https://doi.org/10.1126/science.1204062)
- B.J.R. Davidsson, P.J. Gutiérrez, H. Rickman, Physical properties of morphological units on comet 9p/Tempel 1 derived from near-IR deep impact spectra. *Icarus* **201**(1), 335–357 (2009). doi:[10.1016/j.icarus.2008.12.039](https://doi.org/10.1016/j.icarus.2008.12.039)
- B.J.R. Davidsson, P.J. Gutiérrez, O. Groussin, M.F. A'Hearn, T. Farnham, L.M. Feaga, M.S. Kelley, K.P. Klaasen, F. Merlin, S. Protopapa, H. Rickman, J.M. Sunshine, P.C. Thomas, Thermal inertia and surface roughness of comet 9p/Tempel 1. *Icarus* **224**(1), 154–171 (2013). doi:[10.1016/j.icarus.2013.02.008](https://doi.org/10.1016/j.icarus.2013.02.008)
- B.J.R. Davidsson, H. Rickman, Surface roughness and three-dimensional heat conduction in thermophysical models. *Icarus* **243**, 58–77 (2014). doi:[10.1016/j.icarus.2014.08.039](https://doi.org/10.1016/j.icarus.2014.08.039)
- B.J.R. Davidsson, H. Rickman, J.L. Bandfield, O. Groussin, P.J. Gutiérrez, M. Wilska, M.T. Capria, J.P. Emery, J. Helbert, L. Jorda, A. Maturilli, T.G. Mueller, Interpretation of thermal emission, I: the effect of roughness for spatially resolved atmosphereless bodies. *Icarus* **252**, 1–21 (2015). doi:[10.1016/j.icarus.2014.12.029](https://doi.org/10.1016/j.icarus.2014.12.029)
- M. Delbó, M. Mueller, J.P. Emery, B. Rozitis, M.T. Capria, Asteroid thermophysical modeling. *ArXiv e-prints* (2015)
- M. Delbó, A. Dell'Oro, A.W. Harris, S. Mottola, M. Mueller, Thermal inertia of near-earth asteroids and implications for the magnitude of the Yarkovsky effect. *Icarus* **190**(1), 236–249 (2007). doi:[10.1016/j.icarus.2007.03.007](https://doi.org/10.1016/j.icarus.2007.03.007)
- M. Delbó, G. Libourel, J. Wilkerson, N. Murdoch, P. Michel, K.T. Ramesh, C. Ganino, C. Verati, S. Marchi, Thermal fatigue as the origin of regolith on small asteroids. *Nature* **508**, 233–236 (2014). doi:[10.1038/nature13153](https://doi.org/10.1038/nature13153)
- J.P. Emery, A.L. Sprague, F.C. Witteborn, J.E. Colwell, R.W.H. Kozłowski, D.H. Wooden, Mercury: thermal modeling and mid-infrared (512 μm) observations. *Icarus* **136**(1), 104–123 (1998). doi:[10.1006/icar.1998.6012](https://doi.org/10.1006/icar.1998.6012)
- J.P. Emery, Y.R. Fernández, M.S.P. Kelley, K.T. Warden (née Crane), C. Hergenrother, D.S. Lauretta, M.J. Drake, H. Campins, J. Ziffer, Thermal infrared observations and thermophysical characterization of OSIRIS-REx target asteroid (101955) Bennu. *Icarus* **234**, 17–35 (2014). doi:[10.1016/j.icarus.2014.02.005](https://doi.org/10.1016/j.icarus.2014.02.005)
- R.L. Fergason, P.R. Christensen, H.H. Kieffer, High-resolution thermal inertia derived from the thermal emission imaging system (THEMIS): thermal model and applications. *J. Geophys. Res., Planets* **111**(E12), E12004 (2006). doi:[10.1029/2006JE002735](https://doi.org/10.1029/2006JE002735)
- F.M. Flasar, R.K. Achterberg, B.J. Conrath, J.C. Pearl, G.L. Bjoraker, D.E. Jennings, P.N. Romani, A.A. Simon-Miller, V.G. Kunde, C.A. Nixon, B. Bzard, G.S. Orton, L.J. Spilker, J.R. Spencer, P.G.J. Irwin, N.A. Teanby, T.C. Owen, J. Brasunas, M.E. Segura, R.C. Carlson, A. Mamoutkine, P.J. Gierasch,

- P.J. Schinder, M.R. Showalter, C. Ferrari, A. Barucci, R. Courtin, A. Coustenis, T. Fouchet, D. Gautier, E. Lellouch, A. Marten, R. Prang, D.F. Strobel, S.B. Calcutt, P.L. Read, F.W. Taylor, N. Bowles, R.E. Samuelson, M.M. Abbas, F. Raulin, P. Ade, S. Edgington, S. Pilorz, B. Wallis, E.H. Wishnow, Temperatures, winds, and composition in the saturnian system. *Science* **307**(5713), 1247–1251 (2005). doi:[10.1126/science.1105806](https://doi.org/10.1126/science.1105806)
- T. Fukuhara, M. Taguchi, T. Imamura, M. Nakamura, M. Ueno, M. Suzuki, N. Iwagami, M. Sato, K. Mitsuyama, G.L. Hashimoto, R. Ohshima, T. Kouyama, H. Ando, M. Futaguchi, Lir: Longwave infrared camera onboard the Venus orbiter Akatsuki. *Earth Planets Space* **63**(9), 1009–1018 (2012). doi:[10.5047/eps.2011.06.019](https://doi.org/10.5047/eps.2011.06.019)
- I. Gatley, H. Kieffer, E. Miner, G. Neugebauer, Infrared observations of Phobos from Mariner 9. *Astrophys. J.* **190**, 497–508 (1974). doi:[10.1086/152902](https://doi.org/10.1086/152902)
- M. Grott et al., *Space Sci. Rev.*, this issue (2015)
- O. Groussin, M.F. A'Hearn, J.-Y. Li, P.C. Thomas, J.M. Sunshine, C.M. Lisse, K.J. Meech, T.L. Farnham, L.M. Feaga, W.A. Delamere, Surface temperature of the nucleus of comet 9p/Tempel 1. *Icarus* **187**(1), 16–25 (2007). doi:[10.1016/j.icarus.2006.08.030](https://doi.org/10.1016/j.icarus.2006.08.030)
- O. Groussin, J.M. Sunshine, L.M. Feaga, L. Jorda, P.C. Thomas, J.-Y. Li, M.F. A'Hearn, M.J.S. Belton, S. Besse, B. Carcich, T.L. Farnham, D. Hampton, K. Klaasen, C. Lisse, F. Merlin, S. Protopapa, The temperature, thermal inertia, roughness and color of the nuclei of comets 103P/Hartley 2 and 9P/Tempel 1. *Icarus* **222**(2), 580–594 (2013). *Stardust/EPOXI*. doi:[10.1016/j.icarus.2012.10.003](https://doi.org/10.1016/j.icarus.2012.10.003)
- S. Gulkis, S. Keihm, L. Kamp, S. Lee, P. Hartogh, J. Crovisier, E. Lellouch, P. Encrenaz, D. Bockelee-Morvan, M. Hofstadter, G. Beaudin, M. Janssen, P. Weissman, P.A. von Allmen, T. Encrenaz, C.R. Backus, W.-H. Ip, P.F. Schloerb, N. Biver, T. Spilker, I. Mann, Continuum and spectroscopic observations of asteroid (21) Lutetia at millimeter and submillimeter wavelengths with the MIRO instrument on the Rosetta spacecraft. *Planet. Space Sci.* **66**(1), 31–42 (2012). doi:[10.1016/j.pss.2011.12.004](https://doi.org/10.1016/j.pss.2011.12.004)
- S. Gulkis, M. Allen, P. von Allmen, G. Beaudin, N. Biver, D. Bockelee-Morvan, M. Choukroun, J. Crovisier, B.J.R. Davidsson, P. Encrenaz, T. Encrenaz, M. Frerking, P. Hartogh, M. Hofstadter, W.-H. Ip, M. Janssen, C. Jarchow, S. Keihm, S. Lee, E. Lellouch, C. Leyrat, L. Rezac, F.P. Schloerb, T. Spilker, Subsurface properties and early activity of comet 67p/Churyumov-Gerasimenko. *Science* **347**(6220) (2015). doi:[10.1126/science.aaa0709](https://doi.org/10.1126/science.aaa0709)
- B. Gundlach, J. Blum, A new method to determine the grain size of planetary regolith. *Icarus* **223**(1), 479–492 (2013). doi:[10.1016/j.icarus.2012.11.039](https://doi.org/10.1016/j.icarus.2012.11.039)
- J. Hanuš, M. Delbo, J. Ďurech, V. Alí-Lagoa, Thermophysical modeling of asteroids from WISE thermal infrared data significance of the shape model and the pole orientation uncertainties. *Icarus* **256**, 101–116 (2015). doi:[10.1016/j.icarus.2015.04.014](https://doi.org/10.1016/j.icarus.2015.04.014)
- B. Hapke, Bidirectional reflectance spectroscopy, 3: correction for macroscopic roughness. *Icarus* **59**(1), 41–59 (1984). doi:[10.1016/0019-1035\(84\)90054-X](https://doi.org/10.1016/0019-1035(84)90054-X)
- S. Hasegawa, T.G. Müller, K. Kawakami, T. Kasuga, T. Wada, Y. Ita, N. Takato, H. Terada, T. Fujiyoshi, M. Abe, Albedo, size, and surface characteristics of Hayabusa-2 sample-return target 162173 1999 JU3 from AKARI and Subaru observations. *Publ. Astron. Soc. Jpn.* **60**(sp2), 399–405 (2008). doi:[10.1093/pasj/60.sp2.S399](https://doi.org/10.1093/pasj/60.sp2.S399)
- F. Horz, M. Cintala, Impact experiments related to the evolution of planetary regoliths. *Meteorit. Planet. Sci.* **32**, 179–209 (1997). doi:[10.1111/j.1945-5100.1997.tb01259.x](https://doi.org/10.1111/j.1945-5100.1997.tb01259.x)
- C.J.A. Howett, J.R. Spencer, J. Pearl, M. Segura, Thermal inertia and bolometric bond albedo values for Mimas, Enceladus, Tethys, Dione, Rhea and Iapetus as derived from Cassini/CIRS measurements. *Icarus* **206**(2), 573–593 (2010). doi:[10.1016/j.icarus.2009.07.016](https://doi.org/10.1016/j.icarus.2009.07.016)
- M. Ishiguro, D. Kuroda, S. Hasegawa, M.-J. Kim, Y.-J. Choi, N. Moskovitz, S. Abe, K.-S. Pan, J. Takahashi, Y. Takagi, A. Arai, N. Tokimasa, H.H. Hsieh, J.E. Thomas-Osip, D.J. Osip, M. Abe, M. Yoshikawa, S. Urakawa, H. Hanayama, T. Sekiguchi, K. Wada, T. Sumi, P.J. Tristram, K. Furusawa, F. Abe, A. Fukui, T. Nagayama, D.S. Warjurkar, A. Rau, J. Greiner, P. Schady, F. Knust, F. Usui, T.G. Müller, Optical properties of (162173) 1999 JU3: In preparation for the JAXA Hayabusa 2 sample return mission. *Astrophys. J.* **792**(1), 74 (2014)
- S.J. Keihm, M.G. Langseth Jr., Surface brightness temperatures at the Apollo 17 heatflow site: thermal conductivity of the upper 15 cm of regolith, in *Proceedings of the 4th Lunar Science Conference, vol. 3* (1973), pp. 1503–1513
- S. Keihm, F. Tosi, L. Kamp, F. Capaccioni, S. Gulkis, D. Grassi, M. Hofstadter, G. Filacchione, S. Lee, S. Giuppi, M. Janssen, M. Capria, Interpretation of combined infrared, submillimeter, and millimeter thermal flux data obtained during the Rosetta fly-by of Asteroid (21) Lutetia. *Icarus* **221**(1), 395–404 (2012). doi:[10.1016/j.icarus.2012.08.002](https://doi.org/10.1016/j.icarus.2012.08.002)
- S. Keihm, F. Tosi, M.T. Capria, M.C.D. Sanctis, A. Longobardo, E. Palomba, C.T. Russell, C.A. Raymond, Separation of thermal inertia and roughness effects from Dawn/VIR measurements of Vesta surface temperatures in the vicinity of Marcia crater. *Icarus* **262**, 30–43 (2015). doi:[10.1016/j.icarus.2015.08.028](https://doi.org/10.1016/j.icarus.2015.08.028)

- S.J. Keihm, Interpretation of the lunar microwave brightness temperature spectrum: feasibility of orbital heat flow mapping. *Icarus* **60**(3), 568–589 (1984). doi:[10.1016/0019-1035\(84\)901659](https://doi.org/10.1016/0019-1035(84)901659)
- L. Ksanfomality, S. Murchie, D. Britt, T. Duxbury, P. Fisher, N. Goroshkova, J. Head, E. Kuhrt, V. Moroz, B. Murray, G. Nikitin, E. Petrova, C. Pieters, A. Soufflot, A. Zharkov, B. Zhukov, Phobos: spectrophotometry between 0.3 and 0.6 m and IR-radiometry. *Planet. Space Sci.* **39**(1), 311–326 (1991). doi:[10.1016/0032-0633\(91\)90152-Z](https://doi.org/10.1016/0032-0633(91)90152-Z)
- E. Kührt, B. Giese, H.U. Keller, L.V. Ksanfomality, Interpretation of the krfm-infrared measurements of Phobos. *Icarus* **96**(2), 213–218 (1992). doi:[10.1016/0019-1035\(92\)90075-1](https://doi.org/10.1016/0019-1035(92)90075-1)
- L. Ksanfomality, V. Moroz, P. Bibring, M. Combes, A. Soufflot, O. Ganpantzerova, N. Goroshikova, A. Zharkov, G. Nikiti, E. Petrova, Spatial variations in thermal and albedo properties of the surface of Phobos. *Nature* **341**, 588–591 (1989)
- J.S.V. Lagerros, Thermal physics of asteroids, I: effects of shape, heat conduction and beaming. *Astron. Astrophys.* **310**, 1011–1020 (1996)
- J.S.V. Lagerros, Thermal physics of asteroids, III: irregular shapes and albedo variegations. *Astron. Astrophys.* **325**, 1226–1236 (1997)
- J.S.V. Lagerros, Thermal physics of asteroids, IV: thermal infrared beaming. *Astron. Astrophys.* **332**, 1132–1223 (1998)
- D.S. Lauretta, The OSIRIS-REX team. An overview of the OSIRIS-REX asteroid sample return mission. *Lunar Planet. Sci. Conf. Abstr.* **43**, 2491 (2012)
- E. Lellouch, P. Santos-Sanz, P. Lacerda, M. Mommert, R. Duffard, J.L. Ortiz, T.G. Müller, S. Fornasier, J. Stansberry, C. Kiss, E. Vilenius, M. Mueller, N. Peixinho, R. Moreno, O. Groussin, A. Delsanti, A.W. Harris, TNOS are cool: a survey of the trans-Neptunian region. *Astron. Astrophys.* **557**, 60 (2013). doi:[10.1051/0004-6361/201322047](https://doi.org/10.1051/0004-6361/201322047)
- E. Lellouch, J. Stansberry, J. Emery, W. Grundy, D.P. Cruikshank, Thermal properties of Plutos and Charons surfaces from spitzer observations. *Icarus* **214**(2), 701–716 (2011). doi:[10.1016/j.icarus.2011.05.035](https://doi.org/10.1016/j.icarus.2011.05.035)
- C. Leyrat, A. Coradini, S. Erard, F. Capaccioni, M.T. Capria, P. Drossart, M.C.D. Sanctis, F. Tosi, V. Team, Thermal properties of the asteroid (2867) Steins as observed by Virtis/Rosetta. *Astron. Astrophys.* **531**, 168 (2011). doi:[10.1051/0004-6361/201116529](https://doi.org/10.1051/0004-6361/201116529)
- J.L. Linsky, Models of the lunar surface including temperature dependent thermal properties. *Icarus* **5**(16), 606–634 (1966). doi:[10.1016/0019-1035\(66\)90075-3](https://doi.org/10.1016/0019-1035(66)90075-3)
- S.C. Lowry, P.R. Weissman, S.R. Duddy, B. Rozitis, A. Fitzsimmons, S.F. Green, M.D. Hicks, C. Snodgrass, S.D. Wolters, S.R. Chesley, J. Pittichová, P. van Oers, The internal structure of asteroid (25143) Itokawa as revealed by detection of YORP spin-up. *Astron. Astrophys.* **562**, 48 (2014). doi:[10.1051/00046361/201322602](https://doi.org/10.1051/00046361/201322602)
- J.I. Lunine, G. Neugebauer, B.M. Jakosky, Infrared observations of Phobos and Deimos from Viking. *J. Geophys. Res., Solid Earth* **87**(B12), 10297–10305 (1982). doi:[10.1029/JB087iB12p10297](https://doi.org/10.1029/JB087iB12p10297)
- M.T. Mellon, B.M. Jakosky, H.H. Kieffer, P.R. Christensen, High-resolution thermal inertia mapping from the Mars global surveyor thermal emission spectrometer. *Icarus* **148**(2), 437–455 (2000). doi:[10.1006/icar.2000.6503](https://doi.org/10.1006/icar.2000.6503)
- N.A. Moskovitz, S. Abe, K.-S. Pan, D.J. Osip, D. Pefkou, M.D. Melita, M. Elias, K. Kitazato, S.J. Bus, F.E. DeMeo, R.P. Binzel, P.A. Abell, Rotational characterization of Hayabusa II target asteroid (162173) 1999 JU3. *Icarus* **224**(1), 24–31 (2013). doi:[10.1016/j.icarus.2013.02.009](https://doi.org/10.1016/j.icarus.2013.02.009)
- T.G. Müller, S. Hasegawa, F. Usui, (25143) Itokawa: the power of radiometric techniques for the interpretation of remote thermal observations in the light of the Hayabusa rendezvous results. *Publ. Astron. Soc. Jpn.* **66**, 52 (2014). doi:[10.1093/pasj/psu034](https://doi.org/10.1093/pasj/psu034)
- T.G. Müller, J.S.V. Lagerros, Asteroids as far-infrared photometric standards for ISOPHOT. *Astron. Astrophys.* **338**, 340–352 (1998)
- T.G. Müller, J.S.V. Lagerros, M. Burgdorf, T. Lim, P.M. Morris, A. Salama, B. Schulz, B. Vandenbussche, Fundamental thermal emission parameters of main-belt asteroids derived from ISO. *ESA SP* **427**, 141 (1999)
- T.G. Müller, T. Sekiguchi, M. Kaasalainen, M. Abe, S. Hasegawa, Thermal infrared observations of the Hayabusa spacecraft target asteroid 25143 Itokawa. *Astron. Astrophys.* **443**(1), 347–355 (2005). doi:[10.1051/00046361:20053862](https://doi.org/10.1051/00046361:20053862)
- T.G. Müller, J. Āurech, S. Hasegawa, M. Abe, K. Kawakami, T. Kasuga, D. Kinoshita, D. Kuroda, S. Urakawa, S. Okumura, Y. Sarugaku, S. Miyasaka, Y. Takagi, P.R. Weissman, Y.-J. Choi, S. Larson, K. Yanagisawa, S. Nagayama, Thermo-physical properties of 162173 (1999JU3), a potential flyby and rendezvous target for interplanetary missions. *Astron. Astrophys.* **525**, 145 (2011). doi:[10.1051/0004-6361/201015599](https://doi.org/10.1051/0004-6361/201015599)
- T. Okada et al., *Space Sci. Rev.*, this issue (2015)
- C.P. Opeil, G.J. Consolmagno, D.T. Britt, The thermal conductivity of meteorites: new measurements and analysis. *Icarus* **208**(1), 449–454 (2010). doi:[10.1016/j.icarus.2010.01.021](https://doi.org/10.1016/j.icarus.2010.01.021)

- L. O'Rourke, T.G. Müller, I. Valtchanov, B. Altieri, B.M. González-García, B. Bhattacharya, L. Jorda, B. Carry, M. Küppers, O. Groussin, K. Altwegg, M.A. Barucci, D. Bockelee-Morvan, J. Crovisier, E. Dotto, P. Garcia-Lario, M. Kidger, A. Llorente, R. Lorente, A.P. Marston, M. Sanchez Portal, R. Schulz, M. Sierra, D. Teyssier, R. Vavrek, Thermal and shape properties of asteroid (21) Lutetia from Herschel observations around the Rosetta flyby. *Planet. Space Sci.* **66**(1), 192–199 (2012). doi:[10.1016/j.pss.2012.01.004](https://doi.org/10.1016/j.pss.2012.01.004)
- D.A. Paige, M.C. Foote, B.T. Greenhagen, J.T. Schofield, S. Calcutt, A.R. Vasavada, D.J. Preston, F.W. Taylor, C.C. Allen, K.J. Snook, B.M. Jakosky, B.C. Murray, L.A. Soderblom, B. Jau, S. Loring, J. Bulharowski, N.E. Bowles, I.R. Thomas, M.T. Sullivan, C. Avis, E.M. De Jong, W. Hartford, D.J. McCleese, The Lunar reconnaissance orbiter diviner Lunar radiometer experiment. *Space Sci. Rev.* **150**(1), 125–160 (2010). doi:[10.1007/s11214-009-9529-2](https://doi.org/10.1007/s11214-009-9529-2)
- N.E. Putzig, M.T. Mellon, K.A. Kretke, R.E. Arvidson, Global thermal inertia and surface properties of Mars from the MGS mapping mission. *Icarus* **173**(2), 325–341 (2005). doi:[10.1016/j.icarus.2004.08.017](https://doi.org/10.1016/j.icarus.2004.08.017)
- J.A. Rathbun, J.R. Spencer, L.K. Tamppari, T.Z. Martin, L. Barnard, L.D. Travis, Mapping of Io's thermal radiation by the Galileo photopolarimeter/radiometer (PPR) instrument. *Icarus* **169**(1), 127–139 (2004). Special Issue: Io after Galileo. doi:[10.1016/j.icarus.2003.12.021](https://doi.org/10.1016/j.icarus.2003.12.021)
- B. Rozitis, S.F. Green, Directional characteristics of thermal infrared beaming from atmosphereless planetary surfaces: a new thermophysical model. *Mon. Not. R. Astron. Soc.* **415**(3), 2042–2062 (2011). doi:[10.1111/j.1365-2966.2011.18718.x](https://doi.org/10.1111/j.1365-2966.2011.18718.x)
- J.R. Spencer, The surfaces of Europa, Ganymede, and Callisto: an investigation using Voyager Iris thermal infrared spectra (Jupiter) (1987). <http://hdl.handle.net/10150/184098>
- J.R. Spencer, A rough-surface thermophysical model for airless planets. *Icarus* **83**(1), 27–38 (1990). doi:[10.1016/0019-1035\(90\)90004-S](https://doi.org/10.1016/0019-1035(90)90004-S)
- J.R. Spencer, L.A. Lebofsky, M.V. Sykes, Systematic biases in radiometric diameter determinations. *Icarus* **78**(2), 337–354 (1989). doi:[10.1016/0019-1035\(89\)90182-6](https://doi.org/10.1016/0019-1035(89)90182-6)
- J.R. Spencer, L.K. Tamppari, T.Z. Martin, L.D. Travis, Temperatures on Europa from Galileo photopolarimeter/radiometer: nighttime thermal anomalies. *Science* **284**(5419), 1514–1516 (1999). doi:[10.1126/science.284.5419.1514](https://doi.org/10.1126/science.284.5419.1514)
- T. Spohn, J. Knollenberg, A.J. Ball, M. Banaszekiewicz, J. Benkhoff, M. Grott, J. Grygorczuk, C. Hüttig, A. Hagermann, G. Kargl, E. Kaufmann, N. Kömle, E. Kührt, K.J. Kossacki, W. Marczewski, I. Pelivan, R. Schrödter, K. Seifertlin, Thermal and mechanical properties of the near-surface layers of comet 67P/Churyumov-Gerasimenko. *Science* **349**(6247) (2015). doi:[10.1126/science.aab0464](https://doi.org/10.1126/science.aab0464)
- S.A. Stern, F. Bagenal, K. Ennico, G.R. Gladstone, W.M. Grundy, W.B. McKinnon, J.M. Moore, C.B. Olkin, J.R. Spencer, H.A.L.A. Weaver Young, T. Andert, J. Andrews, M. Banks, B. Bauer, J. Bauman, O.S. Barnouin, P. Bedini, K. Beisser, R.A. Beyer, S. Bhaskaran, R.P. Binzel, E. Birath, M. Bird, D.J. Bogan, A. Bowman, V.J. Bray, M. Brozovic, C. Bryan, M.R. Buckley, M.W. Buie, B.J. Buratti, S.S. Bushman, A. Calloway, B. Carcich, A.F. Cheng, S. Conard, C.A. Conrad, J.C. Cook, D.P. Cruikshank, O.S. Custodio, C.M.D. Ore, C. Deboy, Z.J.B. Dirschner, P. Dumont, A.M. Earle, H.A. Elliott, J. Ercol, C.M. Ernst, T. Finley, S.H. Flanigan, G. Fountain, M.J. Freeze, T. Greathouse, J.L. Green, Y. Guo, M. Hahn, D.P. Hamilton, S.A. Hamilton, J. Hanley, A. Harch, H.M. Hart, C.B. Hersman, A. Hill, M.E. Hill, D.P. Hinson, M.E. Holdridge, M. Horanyi, A.D. Howard, C.J.A. Howett, C. Jackman, R.A. Jacobson, D.E. Jennings, J.A. Kammer, H.K. Kang, D.E. Kaufmann, P. Kollmann, S.M. Krimigis, D. Kusnierkiewicz, T.R. Lauer, J.E. Lee, K.L. Lindstrom, I.R. Linscott, C.M. Lisse, A.W. Lunsford, V.A. Malder, N. Martin, D.J. McComas, R.L. McNutt, D. Mehoke, T. Mehoke, E.D. Melin, M. Mutchler, D. Nelson, F. Nimmo, J.I. Nunez, A. Ocampo, W.M. Owen, M. Paetzold, B. Page, A.H. Parker, J.W. Parker, F. Pelletier, J. Peterson, N. Pinkine, M. Piquette, S.B. Porter, S. Protopapa, J. Redfern, H.J. Reitsema, D.C. Reuter, J.H. Roberts, S.J. Robbins, G. Rogers, D. Rose, K. Runyon, K.D. Retherford, M.G. Ryschkevitch, P. Schenk, P. Schindhelm, B. Sepan, M.R. Showalter, K.N. Singer, M. Soluri, D. Stanbridge, A.J. Steffl, D.F. Strobel, T. Stryk, M.E. Summers, J.R. Szalay, M. Tapley, A. Taylor, H. Taylor, H.B. Throop, C.C.C. Tsang, G.L. Tyler, O.M. Umurhan, A.J. Verbiscer, M.H. Versteeg, M. Vincent, R. Webber, S. Weidner, G.E. Weigle, O.L. White, K. Whittenburg, B.G. Williams, K. Williams, S. Williams, W.W. Woods, A.M. Zangari, E. Zirnstein, The Pluto system: initial results from its exploration by new horizons. *Science* **350**(6258) (2015). doi:[10.1126/science.aad1815](https://doi.org/10.1126/science.aad1815)
- Y. Tsuda, M. Yoshikawa, M. Abe, H. Minamino, S. Nakazawa, System design of the Hayabusa 2 asteroid sample return mission to 1999 JU3. *Acta Astronaut.* **91**, 356–362 (2013). doi:[10.1016/j.actaastro.2013.06.028](https://doi.org/10.1016/j.actaastro.2013.06.028)
- A.R. Vasavada, J.L. Bandfield, B.T. Greenhagen, P.O. Hayne, M.A. Siegler, J.-P. Williams, D.A. Paige, Lunar equatorial surface temperatures and regolith properties from the diviner Lunar radiometer experiment. *J. Geophys. Res., Planets* **117**(E12), E00H18 (2012). doi:[10.1029/2011JE003987](https://doi.org/10.1029/2011JE003987)

- F. Vilas, Spectral characteristics of Hayabusa 2 near-Earth asteroid targets 162173 1999 JU3 and 2001 QC34. *Astron. J.* **135**(4), 1101 (2008)
- D. Vokrouhlický, A. Milani, S.R. Chesley, Yarkovsky effect on small near-Earth asteroids: mathematical formulation and examples. *Icarus* **148**(1), 118–138 (2000). doi:[10.1006/icar.2000.6469](https://doi.org/10.1006/icar.2000.6469)
- K. Yomogida, T. Matsui, Physical properties of ordinary chondrites. *J. Geophys. Res., Solid Earth* **88**(B11), 9513–9533 (1983). doi:[10.1029/JB088iB11p09513](https://doi.org/10.1029/JB088iB11p09513)